THESIS FOR THE DEGREE OF DOCTOR OF PHILOSOPHY IN SOLID AND STRUCTURAL MECHANICS

Influence of rail, wheel and track geometries on wheel and rail degradation

KALLE KARTTUNEN

Department of Applied Mechanics
CHALMERS UNIVERSITY OF TECHNOLOGY

Göteborg, Sweden 2015

Influence of rail, wheel and track geometries on wheel and rail degradation
KALLE KARTTUNEN
ISBN 978-91-7597-203-9

Doktorsavhandlingar vid Chalmers tekniska högskola
Ny serie nr. 3884
ISSN 0346-718X
Department of Applied Mechanics
Chalmers University of Technology
SE-412 96 Göteborg
Sweden
Telephone: +46 (0)31-772 1000

Chalmers Reproservice
Göteborg, Sweden 2015

Influence of rail, wheel and track geometries on wheel and rail degradation
Thesis for the degree of Doctor of Philosophy in Solid and Structural Mechanics
KALLE KARTTUNEN
Department of Applied Mechanics
Chalmers University of Technology

Abstract

For more efficient railway maintenance there is a need to increase the understanding of the influence of operational conditions on wheel and rail degradation. To this end, the chosen primary investigation strategy is to employ dynamic multibody simulations, where operational conditions are altered, to estimate the influence on material deterioration. Operational conditions considered are track, wheel and rail geometries; and types of material deterioration that are considered are rolling contact fatigue (RCF) and wear.

Track geometry, especially the curve radius, has a large influence on wheel/rail degradation. Smaller curve radii lead to higher degradation. By also considering the influence of lateral track irregularities in curves, a more complicated relationship emerge. Large curve radii and a high level of lateral irregularities lead to an increase in RCF over the length of a curve. For small radius curves, where wear is the dominating damage mechanism, an increase in the level of lateral irregularities leads to a transition towards a mixed RCF/wear regime for the outer (high) rail.

The influence of wheel and rail geometries on degradation is studied by parametrisation of wheel/rail geometries, employing a design of experiments scheme to the multibody simulations that determine degradation, and finally by deriving meta-models through regression analysis. The meta-models link estimated degradation magnitudes to key geometric parameters. The advantage of the meta-models is that degradation magnitudes can be evaluated with a very low computational cost. This has the benefit that measured wheel and rail profiles can be ranked based on how detrimental they are. Examples are presented for altered gauge corner and flange root geometries, and also for hollow worn wheels.

A field study of RCF of locomotive wheels shows its strong dependence on operational conditions. Seasonal variations in the number of wheel reprofilings are explained in terms of seasonal variations in weather conditions, lubrication practices and rail grinding.

Keywords: Rolling contact fatigue, wear, rolling contact, railway, wheel, rail, track geometry, maintenance

Preface

The work presented in this thesis has been carried out between October 2010 and May 2015 at the Department of Applied Mechanics at Chalmers University of Technology. It has been part of the project MU27 "Progressive degradation of wheels and rails" within the Swedish National Centre of Excellence in Railway Mechanics (CHARMEC).

Acknowledgements

I would like to start by giving many thanks to my main supervisor Elena Kabo. I'm especially grateful over that you do not micromanage although you do notice microscopic things that need to be corrected. Also my co-supervisor Anders Ekberg deserves many thanks. To show optimism over what other would classify as small progresses is remarkable trait to have.

I would also like to show gratitude to the reference group members, including Viktor Berbyuk, Simon Gripner, Roger Lundén, Arne Nissen and Thomas Svensson. Special thanks to Simon and Arne for the help with track measurement data. Thanks to the members of the parallel CHARMEC project MU26 Emil Gustavsson, Ann-Brith Strömberg and co-supervisor Michael Patriksson. Ingemar Persson deserves also many thanks for the help with GENSYS. Björn Pålsson and Peter Torstensson are acknowledged for their help.

The past and present room mates, Anders T. Johansson, Majid Khorsand Vakilzadeh and Sadegh Rahrovani deserve a special mention. It has been a pleasure to share an office with all of you. Finally, thanks to the friends and colleagues at the divisions of Dynamics and Material & Computational Mechanics for providing a nice work environment.

Göteborg, May 2015

Kalle Karttunen

Nomenclature

$\boldsymbol{\beta}$	Vector containing the regression parameters (coefficients of meta-models).
γ_{x}	Longitudinal creep [-].
γ_{y}	Lateral creep [-].
$\mathbf{X}$	Design matrix (each row corresponds to one scenario).
μ	Coefficient of friction [-].
θ	Inclination of the ellipses describing the hollow worn wheel [rad].
a	Major semi-axis of the elliptical contact area [m].
a_{e1}	Major axis of the ellipse on the field side of the hollow worn wheel [m].
a_{e2}	Major axis of the ellipse on the flange side of the hollow worn wheel [m].
a_i	Coefficient of a general second degree equation, $i = \{r, w\}$, where r represents the rail and w the wheel. Rail and wheel profiles measured in millimetres.
b	Minor semi-axis of the elliptical contact area [m].
b_{e}	Minor axis of the ellipses of the hollow worn wheel [m].
b_i	Coefficient of a general second degree equation, $i = \{r, w\}$, where r represents the rail and w the wheel. Rail and wheel profiles measured in millimetres.
c_i	Coefficient of a general second degree equation, $i = \{r, w\}$, where r represents the rail and w the wheel. Rail and wheel profiles measured in millimetres.
d_i	Coefficient of a general second degree equation, $i = \{r, w\}$, where r represents the rail and w the wheel. Rail and wheel profiles measured in millimetres.
e_i	Coefficient of a general second degree equation, $i = \{r, w\}$, where r represents the rail and w the wheel. Rail and wheel profiles measured in millimetres.
f	Traction coefficient [-].
F_{x}	Longitudinal component of the tangential contact force [N].
F_{y}	Lateral component of the tangential contact force [N].
F_{z}	Total contact load in normal direction [N].
f_i	Coefficient of a general second degree equation, $i = \{r, w\}$, where r represents the rail and w the wheel. Rail and wheel profiles measured in millimetres.
FI_{surf}	Fatigue index for surface initiated rolling contact fatigue [-].
h_{d}	Cant deficiency in [m] for Paper C and in [mm] for Paper D.
k	Work hardened yield strength in shear [Pa].
N_{f}	Fatigue life in number of load cycles.
p	Normal pressure [Pa].
p_0	Maximum normal pressure [Pa].
Q_0	Static vertical wheel force [kN].

q_0	Maximal traction [Pa].
R_1	Radius of the transition circle on field side of the hollow worn wheel [m].
R_2	Radius of the transition circle on flange side of the hollow worn wheel [m].
R_c	Curve radius [m].
$T\gamma$	Dissipated energy, wear number (tangential contact forces multiplied with creep) [N].
Y_{2m}	Track shift force evaluated as a 2 metre moving average [kN].

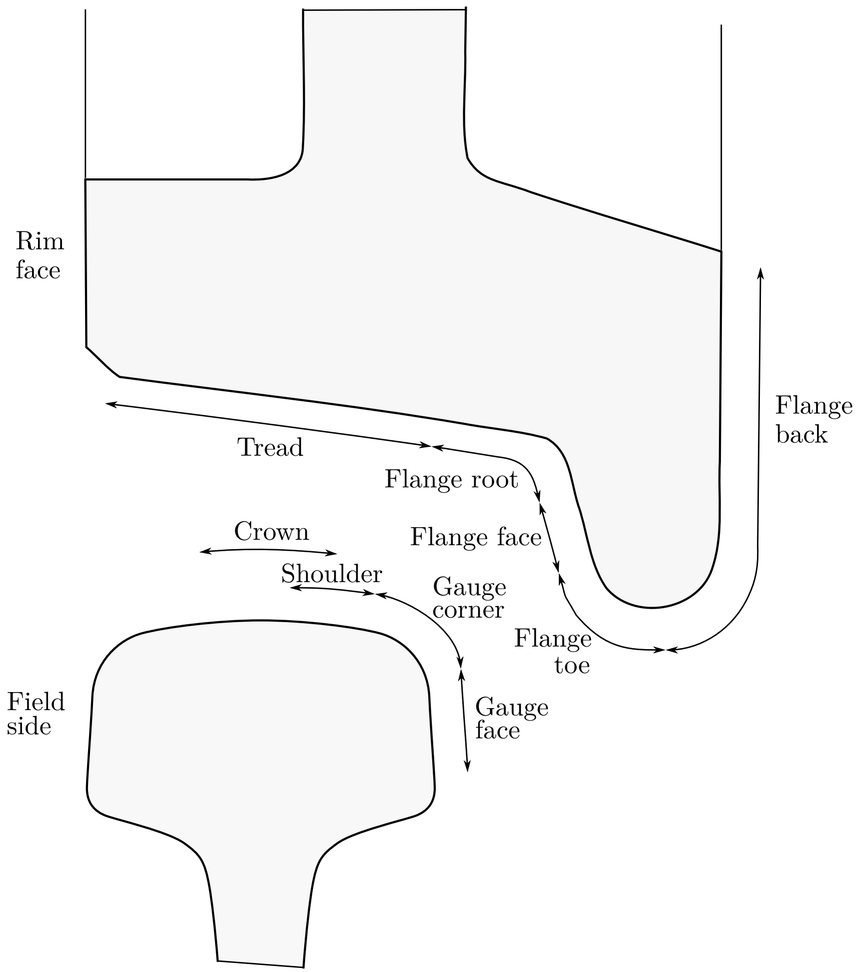

Figure i: *Nomenclature of parts of the wheel rim and rail head.*

Thesis

This thesis consists of an extended summary and the following appended papers:

Paper A	K. Karttunen, E. Kabo, and A. Ekberg [2012]. A numerical study of the influence of lateral geometry irregularities on mechanical deterioration of freight tracks. *Proceedings of the Institution of Mechanical Engineers, Part F: Journal of Rail and Rapid Transit* 226 [6], 575–586. DOI: 10.1177/0954409712445115
Paper B	K. Karttunen, E. Kabo, and A. Ekberg [2014b]. The influence of track geometry irregularities on rolling contact fatigue. *Wear* 314 [1-2], 78–86. DOI: 10.1016/j.wear.2013.11.039
Paper C	K. Karttunen, E. Kabo, and A. Ekberg [2014a]. Numerical assessment of the influence of worn wheel tread geometry on rail and wheel deterioration. *Wear* 317 [1-2], 77–91. DOI: 10.1016/j.wear.2014.05.006
Paper D	K. Karttunen [2015]. "Estimation of gauge corner and flange root degradation from rail, wheel and track geometry". To be submitted for international publication
Paper E	A. Ekberg, E. Kabo, K. Karttunen, et al. [2014]. Identifying the root causes of damage on the wheels of heavy haul locomotives and its mitigation. *Proceedings of the Institution of Mechanical Engineers, Part F: Journal of Rail and Rapid Transit* 228 [6], 663–672. DOI: 10.1177/0954409714526165

The appended papers were prepared in collaboration with the co-authors. The author of this thesis was responsible for the major progress of work in **Paper A** to **Paper C**, i.e. planning the papers, carried out the numerical analyses, and had the main responsibility for writing the papers. In **Paper E** the author of this thesis was responsible for the analysis of the influence of altered rail profile geometries.

Contents

Part I
Extended Summary

1 Introduction

1.1 Background

> "Skenornas nötning på jernväg beror på många omständigheter, och kan endast bestämmas genom gjorda iakttagelser på redan en längre eller kortare tid begagnade jernvägar. För hvarje 1000:de skålpundfot[1] verkställdt mekaniskt arbete uppkommer vid medelhårdt jern en vigtsförlust af 0,0131 à 0,0164 ort. Vid vanlig friktion af jern mot jern är, vid långsam rörelse, vigtförlusten 0,0065 à 0,0098 ort för hårdt, och 0,0164 à 0,0197 ort för mjukt jern. Verka ångvagnens drifhjul häftigt på en och samma del af skenan, och om värmeutveckling tillika uppstår, så kan förlusten uppgå ända till 0,0196 à 0,0338 ort. "

The above quote is from a treatise by Nerman [1856] which is in turn based on a work by Becker [1855]. By no coincidence, the year 1856 is also the year when operation started of sections of the first main lines in Sweden. Some of the key points of the quote are

- wear of rails depends on many factors and can only be determined by observations over time
- a measure of energy is linked to the amount of wear
- the amount of wear is related to the hardness of the rail
- thermal effects caused by wheel slip lead to high wear rates.

The present thesis elaborates on the first point and also includes aspects of rolling contact fatigue (RCF) and wheel damage. The main aims are to identify key (geometrical) factors that influence degradation of rails and wheels, and to quantify their influence.

The degradation levels of wheels and rails are mainly determined by observations. In Sweden the track geometry, transversal rail profile, ballast geometry and rail corrugation are measured at least once a year for most track sections (Trafikverket [2012]). Wayside wheel profile measuring stations have also made their entrance (Asplund et al. [2014]). On top of that there are wheel impact force and hot wheel/axle box detectors which are currently employed in decisions of stopping trains for safety reasons. This means that there are significant amounts of data which can be employed in maintenance planning, especially if condition based preventive maintenance is the preferred paradigm. Already today data of these types are to some extent employed in maintenance planning. For example in European standards both safety and quality limits are stated where the level of track geometry degradation decides whether maintenance has to be either planned (preventive maintenance) or carried out immediately (corrective maintenance), see Section 2.2. Another option for preventive maintenance is predetermined maintenance where

[1] The energy to lift one pound the distance of one foot (pound in Swedish = skålpund = 100 ort = 425.1 grams).

the maintenance schedule is determined by the passage of a certain amount of time or by some parameter based on the actual usage. Since many maintenance actions have to be planned well ahead of time not to cause (excessive) traffic disturbances and also to allow bundling of different maintenance tasks, it is necessary to be able to predict the level of degradation of the object.

As noted above, both rail and wheel profile geometries are currently measured. This gives an opportunity to single out profiles which have high degradation rates. Fröhling, Spangenberg, and Hettasch [2012] showed that removing 7% of the most detrimental wheel profiles, eliminated 84% of the studied wheel/rail profile combinations with high contact stresses. From this, it is clear that it would be useful to have a tool with which wheel and rail profiles can be ranked from benign to detrimental.

When it comes to prediction of degradation of rails and wheels in service, the focus has been mainly on wear of wheels see e.g. Braghin et al. [2006], Jendel [2002], and Pearce and Sherratt [1991]. The previous references have a common approach to predict the shape of the worn wheel profile, namely that multibody simulations are employed to yield wheel/rail contact responses which are thereafter employed in a wear model which in turn updates the wheel profile geometry. These types of simulations are rather complicated and time consuming. Prediction of rail wear through simulations is not as common, but there are examples where wear of both wheel and rail are evaluated simultaneously, see e.g. Ignesti et al. [2014] and Zobory [1997].

1.2 Scope and aim

As mentioned, the main purpose of this thesis is to identify the most significant factors that influence the degradation of wheels and rails, and to derive models that quantify their influence. Degradation mechanisms that are considered are rolling contact fatigue and wear.

To this end, dynamic multibody simulations are employed. Considered operational parameters relate to track, rail and wheel geometries. To limit the (already extensive) complexity, all simulations feature a single wagon (i.e. not several wagons coupled together) and the results are extracted from the leading axle of the first bogie. The robustness of the approach is finally investigated by comparison to similar analysis where another vehicle model is employed.

There are of course limitations with this methodology. The railway is an open system which means that there are many factors, such as weather, train drivers etc., that are not accounted for in the simulations. An example of how seemingly identical locomotives have large variations of running distances between wheel reprofilings is seen in **Paper E**. This shows that there are operational parameters that greatly influence the degradation of wheels which are normally not captured in an assessment. Another limitation is that the influence of different steel grades on degradation has been disregarded. There are also simplifications when it comes to the level of detail of wheel/rail contact modelling and contact force calculations. With these limitations in mind, it should be noted that the results of this thesis are mainly used for comparative purposes. As an example, the meta-models derived to quantify degradation magnitudes in **Paper C** and **Paper D** are used to rank profiles from benign to detrimental, rather than to quantify operational lives.

2 Track geometry and track geometry degradation

2.1 Track geometry and irregularities

The geometry of a track can be seen as a nominal geometry with superposed irregularities. The nominal track geometry consists of vertical curvature, horizontal curvature, gradient (i.e. slope of track), track gauge and cross level (cant). Track irregularities are defined as deviations from this nominal (designed) track geometry. Definitions of track geometry and irregularities are found in CEN [2008]. A selection of the definitions are reiterated below.

- Longitudinal level or vertical alignment: vertical deviation of the running table[1] from the reference line[2]. Measured for both rails.
- Lateral alignment or alignment: lateral deviation of both rails measured from a point between 0 to 14 mm below the running surface[3], see also Figure 2.1.
- Track gauge: track gauge is the shortest distance between the rails measured between 0 to 14 mm below the running surface, see also Figure 2.2.
- Cross level: cross level is evaluated from the angle between the running surface and a horizontal reference plane. It is expressed as the vertical distance between the rails for a hypotenuse of 1500 mm for a nominal gauge of 1435 mm. For curved tracks cross level is often referred to as cant.
- Twist: the rate of change of cross level.

2.2 Quantification of degraded track geometry

A number of ways of quantifying track geometry degradation are defined in norms and standards. Historically these norms and standards were specific for each country. In this section permissible levels for isolated defects and track qualities are given as defined in European standards (which are, or are in progress to become, national standards for many European countries). In general the purpose of the permissible levels of the isolated defects are to ensure that the safety is not jeopardised whilst permissible levels for track quality are used to ensure that ride comfort does not become unacceptable.

[1] Upper surface of the rail head.

[2] Mean position evaluated over different lengths depending on whether isolated defects or track quality measures are assessed.

[3] Surface tangential to the running tables of left and right rails.

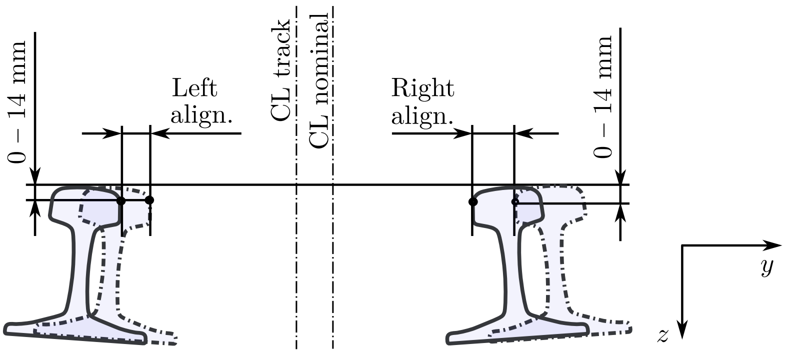

Figure 2.1: *Lateral alignment as defined in CEN [2008]. Dash-dotted rail profile represents the nominal (mean) position of the rail.*

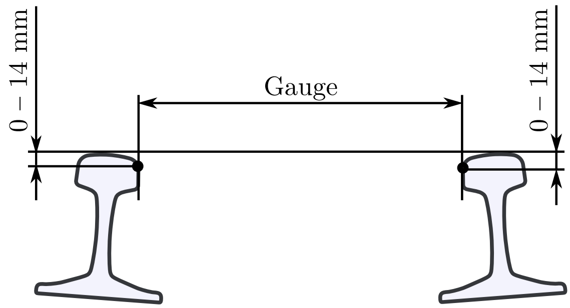

Figure 2.2: *Track gauge as defined in CEN [2008].*

2.2.1 Isolated defects

CEN [2010] defines limits on isolated track geometry defects before an action needs to be taken. The actions are:

- Immediate Action Limit: if the immediate action limit is exceeded, mitigation actions have to be taken immediately (e.g. immediate tamping, closing of the line, or reduced speed limits).
- Intervention Limit: if the intervention limit is exceeded, corrective maintenance has to be performed in order to ensure that the immediate action limit is not reached before the next inspection.
- Alert Limit: if the alert limit is exceeded, correction of track geometry has to be considered in the regular planning of maintenance operations.

Of these, only the immediate action limits are given as binding values in the standard. The other two limits are provided as guidelines for maintenance planning. In Table 2.1 immediate action limits and alert limits for lateral alignment are given. The alert limit values are roughly half of the immediate action limit values. Derailment risks assessed by multibody simulations in D-RAIL [2013] imply that the immediate action limits may not be restrictive enough for defects shorter than 8 metres.

Table 2.1: Immediate action limits and alert limits for lateral aligment at an isolated defect with a wavelength between 3 and 25 metres (CEN [2010]). The mean value should be calculated over a length of at least 50 metres.

Speed [km/h]	Immediate action limit	Alert limit
	Mean to Peak value [mm]	Mean to Peak value [mm]
$v \leq 80$	22	12 to 15
$80 < v \leq 120$	17	8 to 11
$120 < v \leq 160$	14	6 to 9
$160 < v \leq 230$	12	5 to 8
$230 < v \leq 300$	10	4 to 7

2.2.2 Track quality measures

Track geometry quality is commonly quantified by the standard deviation of irregularities over a specified length. Maximum permissible values of the standard deviation for track irregularities are related to the maximum line speed and classification of the track. The European standard prEN 13848-6, see CEN [2012], presents limits on the standard deviations for longitudinal level and alignment as presented in Table 2.2. Limits and track quality classes were obtained by surveying track qualities around Europe.

Table 2.2: Limit of standard deviation of alignment (in [mm]) according to CEN [2012] (average of the standard deviations of left and right rails).

Speed [km/h]	Track quality class				
	A	B	C	D	E
$v \leq 80$	< 0.90	1.25	1.95	2.7	> 2.70
$80 < v \leq 120$	< 0.50	0.70	1.05	1.45	> 1.45
$120 < v \leq 160$	< 0.45	0.55	0.75	1.00	> 1.00
$160 < v \leq 230$	< 0.40	0.50	0.70	0.90	> 0.90
$230 < v \leq 300$	< 0.35	0.40	0.50	0.65	> 0.65
$v > 300$	N/A	N/A	N/A	N/A	N/A

2.2.3 Track shift forces

The lateral track shift force is the total lateral force induced by the wheelset on the track (see Figure 2.3). High track shift forces may lead to large permanent deformations of the track. Therefore a limit criterion has been proposed in UIC [2009]. According to this criterion the 2 metre moving average of the track shift force $Y_{2\mathrm{m}}$ [kN] may not exceed

$$Y_{2\mathrm{m}} \leq K \left(10 + \frac{2Q_0}{3} \right) \tag{2.1}$$

where $K = 0.85$ for freight wagons and $K = 1$ for passenger vehicles. Furthermore, Q_0 [kN] is the static vertical wheel force.

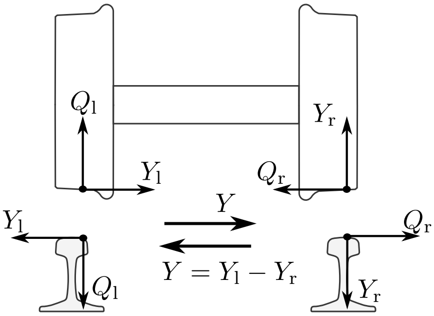

Figure 2.3: *Definition of lateral track shift force Y, vertical wheel force (Q_l, Q_r; left and right respectively) and lateral wheel force (Y_l, Y_r). View in the rolling direction of the wheelset.*

2.3 Characteristics of track geometry degradation

Track geometry degradation may be caused by a re-arrangement of ballast particles due to loads and vibrations from passing train. Tamping restores the track geometry but at the same time tamping causes damage to the track ballast (Audley and Andrews [2013]). The loss of angularity of the ballast particles due to tamping actions leads to increased degradation rates over time since the interlocking between the particles is not as effective when the ballast stones become more rounded (Paderno [2009]).

The characteristics of track geometry degradation was investigated in ORE [1988]. Some of the conclusions are reiterated below:

- both the vertical and lateral alignment degrade linearly with tonnage or time between maintenance operations after the first initial settlement. This trend is not always seen for sections with high degradation rates.
- the rate of degradation is very different from section to section even for apparently identical sections carrying the same traffic.

The first item in the list above is illustrated in Figure 2.4 which shows how the deterioration rate becomes more or less linear after an initial period of a high degradation rate. The first two items have further been demonstrated by Andrade and Teixeira [2011] for a Portuguese rail line. Furthermore the second item is validated by Arasteh khouy et al. [2014] where a distribution of longitudinal degradation rates for the Iron Ore Line in Sweden is presented. Some locations on the line have exceptionally high degradation rates in comparison to the main part of the line. Seasonal variations in the number of track geometry faults were also reported.

Measured standard deviations of the longitudinal level are reported in Esveld [2001] to increase at a mean rate between 0.7 to 2.0 mm per 100 MGT (million gross tonnes).

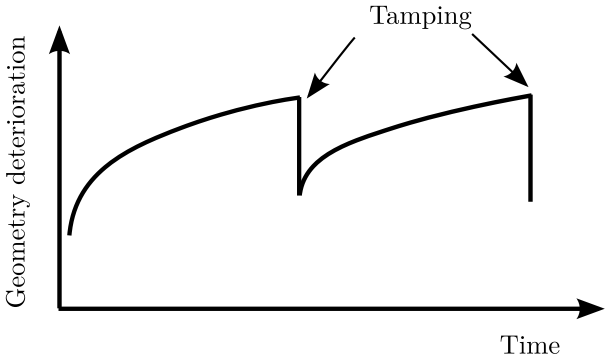

Figure 2.4: *Schematic illustration of track geometry degradation over time.*

In comparison, the standard deviation of the lateral alignment increases at a mean rate between 0.3 to 0.8 mm per 100 MGT. In cases where both the mean vertical and mean lateral degradation rates are presented (Esveld [2001]), the vertical degradation rate is between 1.4 to 3.7 times higher than the lateral rate. For the Iron Ore Line in Sweden similar longitudinal degradation rates have been presented by Arasteh khouy et al. [2014] although, as mentioned above, some sections of the track may have much higher longitudinal degradation rates. Also shown in Arasteh khouy et al. [2014] is that tamping does not restore the track to a perfect nominal geometry, and that there is a considerable variation in the effectiveness of individual tamping actions.

3 Material deterioration of rails and wheels

3.1 Rolling contact fatigue

3.1.1 Common features of RCF

Fatigue damage development can in general be divided into four phases (Tunna, Sinclair, and Perez [2007]). The first phase is crack initiation, the second phase early crack propagation, the third phase extended crack propagation, and the fourth phase final fracture. After the second phase, surface initiated cracks should be visible to the naked eye. The fourth phase – final fracture – may imply anything from a small piece of material detaching to total loss of structural integrity.

The initiation of cracks is dependent on load characteristics, since the material subjected to rolling contact can respond in four different ways depending on the loading (see Johnson [1989] and Figure 3.1):

1. *Elastic response.* If the yield stress of the material is not exceeded the (global) behaviour will be elastic.

2. *Elastic shakedown.* An elastic response is obtained after the yield stress is exceeded in the initial load cycle(s).
3. *Plastic shakedown.* A closed plastic stress–strain loop is formed with no net accumulation of (uni-directional) plastic strain.
4. *Ratcheting.* Incremental (uni-directional) strain accumulation with each load cycle.

The first item in the above list requires the most number of load cycles to initiate a crack whereas the last item requires the fewest number of load cycles. However due to the compressive loading in rolling contact, the number of cycles spent in initiation and early crack growth may even under ratcheting conditions be a substantial portion of the total RCF life as demonstrated with twin disk experiments by Garnham and Davis [2011].

If the material in a rolling contact deforms plastically at the initial load cycle, an elastic response may occur in subsequent load cycles (Johnson [1989]) due to

- protective residual stresses created by the initial plastic deformation that suppresses subsequent yielding;
- strain hardening which raises the yield stress of the material, and
- geometric changes of the surfaces in contact that may result in a more conform contact and thereby lowering the intensity of the contacting stress – so-called wear-in.

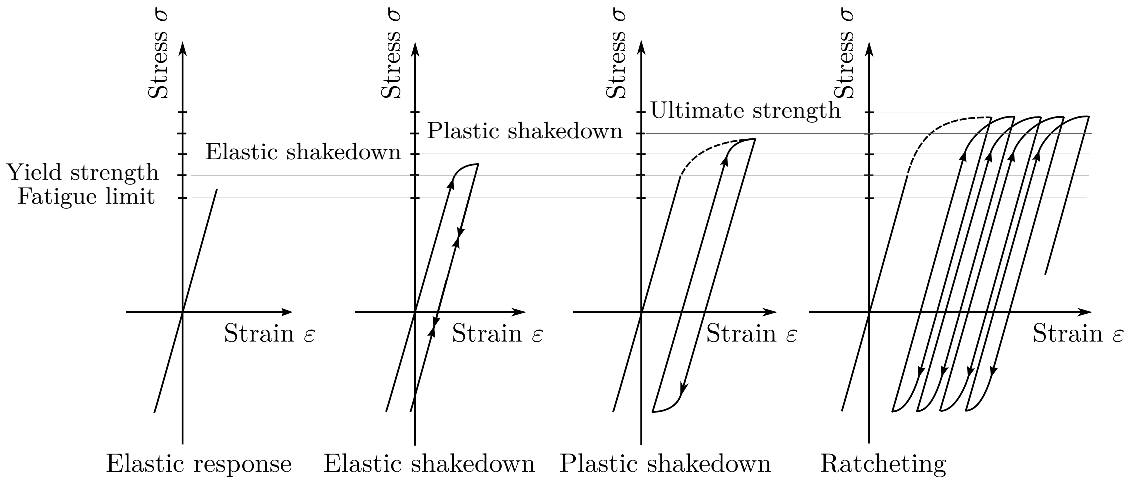

Figure 3.1: *Material responses at different load levels.*

Surface initiated RCF cracks

For a frictional contact between wheel and rail, surface initiated RCF cracks are commonly caused by ratcheting. Due to the accumulation of plastic strain, a crack will form when the fracture strain is exceeded (ductile fracture). Note that in rolling contact the fracture strain is significantly higher than in uni-axial tension due to beneficial compressive stresses (Ekberg and Kabo [2005]). If the tangential contact loads are alternating (i.e. in a case of bi-directional traffic on a rail, or for contact in the running band of a wheel operating in two directions), then no net accumulation of uni-directional plastic strains will occur. In such cases plastic shakedown may occur and crack initiation mechanism will instead be of a low-cycle fatigue type.

Propagation of surface initiated cracks caused by ratcheting is highly influenced by the orientation of the deformed microstructure, see Ekberg and Sotkovszki [2001] and Schilke, Larijani, and Persson [2014]. This commonly means that the crack initially propagates at a shallow angle to the surface and thereafter deviates towards a direction perpendicular to the surface. In wheels, the perpendicular (radial) cracks typically deviate or branch to propagate in a circumferential direction at a depth of 0.5 to 3 mm below the surface (Ekberg and Kabo [2005]). Final fracture occurs when the crack joins adjacent crack(s) whereby a piece of the tread material may be broken off.

Extended crack propagation is believed to be driven by shear stresses with aid from hydraulic mechanisms (Fletcher, Franklin, and Kapoor [2009]). For shear stress driven (mode II propagation, see Figure 3.2) the passing contact load induces shear loads at the crack which will drive crack propagation. Presence of liquids, will lower the crack face friction and may add hydraulic pressurisation, which causes additional mode I loading of the crack. Bower [1988] describes the fluid entrapment and hydraulic pressure transmission mechanisms; a squeeze film fluid mechanism is described by Bogdański [2002].

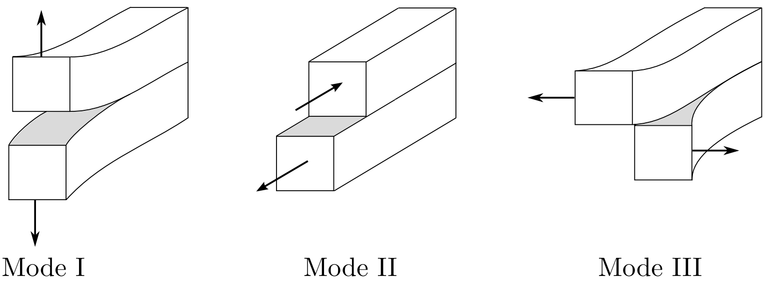

Figure 3.2: *Modes of crack propagation. Mode I is the tensile opening mode, mode II is the (in-plane) shearing mode and mode III the tearing mode.*

Sub-surface initiated RCF cracks

Sub-surface cracks initiate 4 to 25 mm below the surface (Ekberg [2009]). Maximum shear stresses are located below the surface if the coefficient of friction low. Large shear stresses together with material imperfections determines critical crack initiation locations. It should be remembered that the initiation takes place under a multi-axial state of stress. Sub-surface initiated RCF is mainly a high cycle fatigue phenomenon since limited plastic deformation takes place. Cracks initiated deep below the surface are more related to vertical load magnitudes and material defect sizes whereas cracks initiated closer to the surface are more related to contact conditions (Ekberg, Kabo, and Andersson [2002]). Sub-surface initiated RCF cracks are not considered in the current thesis. The interested reader is referred to Ekberg [2000] and references therein.

3.1.2 RCF of rails

The most common form of surface initiated RCF damage to rails are head checks. Head check cracks are manifested as closely spaced cracks of similar direction and size on the gauge corner (UIC [2002]). They are caused by a combination of high normal and tangential stresses at the wheel/rail contact. The stresses cause severe shearing of the surface layer of the rail that leads to fatigue and/or exhaustion of the ductility of the material (ratcheting). The initial microscopic cracks propagate at a shallow angle through the plastically deformed (anisotropic) material of the surface layer. The depth of this anisotropic surface layer has been shown experimentally to be between 1 to 5 mm depending on the hardness of the rail (Jaiswal [2009]). When the crack has grown to a depth where there is no significant plastic deformation of the (isotropic) material, crack propagation may continue in different directions. If the cracks branch towards the surface (or merge with other cracks), parts of the surface material may detach. This is commonly called spalling and is regarded as a relatively harmless form of damage. If instead the crack grows and propagates downwards the end result may be a transverse failure of the rail, see Figure 3.3. Needless to say, such a failure may have serious consequences especially if several transverse fractures occur within a limited section of the track. This was the case for the severe accident at Hatfield, see Smith [2003].

Head checks at the gauge corner are also referred to as gauge corner cracks. Crack mouths are generally oriented perpendicular to the acting creep forces (Magel [2011]). The cracks may occur on long stretches of the rail (e.g. throughout a curve) or found in clusters (e.g. due to track irregularities). The spacing between cracks have been experimentally shown by Stock and Pippan [2014] to decrease with increasing hardness of the rail material. It was also reported that the cracks become more fragmented with increasing hardness.

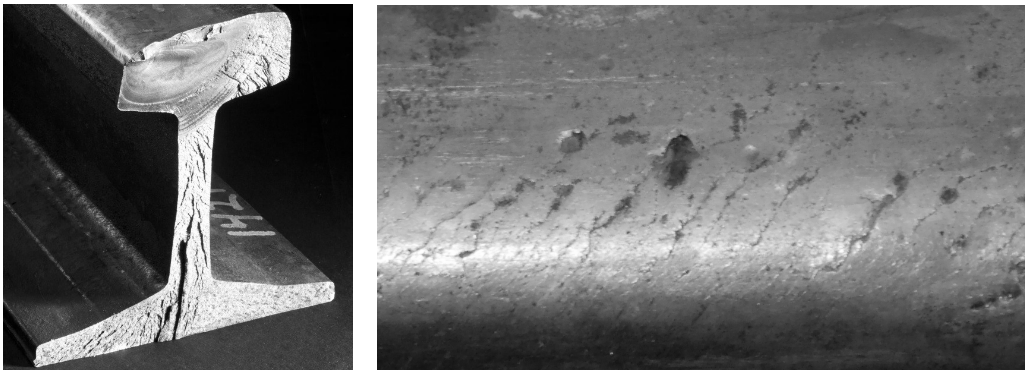

Figure 3.3: *On the left, a rail break caused by a downwards propagating crack (Image courtesy of Jan-Olof Yxell, Chalmers). On the right, gauge corner of the same rail with head checks and spalling (Image courtesy of Magnus Ekh, Chalmers).*

On the Iron Ore Line in Sweden (with 30 tonnes axle loads) eddy current measurements have been performed for sections of the track between 2008 and 2011, see Gustafsson [2012]. Head checks were found basically at every curve with a radius below 700 metres.

At that time grinding was performed once a year for an annual traffic of 30 MGT. On Canadian railways it has been found that head checks may appear after 15 MGT of traffic on newly laid rails (Magel et al. [2003]). On German railways it is reported in Heyder and Brehmer [2014] that head checks are formed after 5 to 10 MGT of traffic . Also the depth of head check cracks is found to increase at a rate of 0.8–2.8 mm/100 MGT for R260[1] rail steels and 0.1–1.2 mm/100 MGT for R350HT[2] rail steels (Heyder and Brehmer [2014]).

Another type of a surface initiated RCF damage is a squat. Squats and squat-type defects have from the outside an appearance of a dark spot, which has the shape of two lungs with surface breaking cracks of V,U,Y or circular shapes. Furthermore, there is a widening of the running band, see Steenbergen and Dollevoet [2013] and UIC [2002]. There are usually two cracks evolving into the rail, one longer crack propagating in the main direction of train operation and one shorter crack propagating in the opposite direction. A distinction is made between squats and squat-type defects by Grassie [2012]. A squat is a surface-initiated RCF defect originating from the plastically deformed surface layer close to or at the gauge corner. A squat-type defect (denoted a stud in Grassie et al. [2012]) is either associated with a white etching layer acting as a initiator or believed to be initiated by high dynamic loads resulting from isolated irregularities on the rail crown. For both squats and squat-type defects the driving traction of the trains have been linked as a possible cause of formation. According to Grassie [2012] it takes only few tens of MGT of traffic to initiate a squat but at least a total of 100 MGT of traffic is required for a squat that is detectable by ultrasonic testing. On the heavy haul Iron Ore Line in Sweden, squat-type defects have been found on the inner rail of curves with a radius of 500 metres and smaller, see Gustafsson [2012][3].

Sub-surface fatigue damage in rails, such as tache ovale (kidney-shaped fatigue) cracks are nowadays rare due to improved steel cleanliness (Fletcher, Franklin, and Kapoor [2009]). The fatigue crack initiation is commonly due to hydrogen embrittlement and/or due to inclusions in the material (Stone [2004]).

3.1.3 RCF of wheels

Surface-initiated RCF cracks are commonly classified based on their appearance and location on the wheel, see e.g. Deuce [2007]. Initially surface initiated RCF damage consists of closely spaced cracks at an angle determined by the loading etc. At later stages pieces of material may break loose due to cracks merging. Zone 1 (field side of the tread) RCF cracks are the most common form of wheel RCF. An example of zone 1 RCF cracks is shown in Figure 3.4. Zone 1 RCF cracks are caused when the wheel is running on the inner rail in curves. The crack mouths are oriented perpendicular to the direction of the resulting tangential contact force during curving. This usually means an orientation of some 30 – 45 degrees towards the wheel axis, see Deuce [2007] and Stone [2004]. Due to the relatively constant longitudinal and lateral contact forces, the material of the wheel at zone 1 experiences uni-directional strain accumulation which may cause ratcheting.

[1] With a minimum ultimate strength of 880 MPa.

[2] Head hardened rail with a minimum ultimate strength of 1175 MPa.

[3] The defects in the source are called squats but since the defects occur at the inner rail of a heavy haul line the defects are here classified as squat-type defects following Grassie [2012].

The inner wheel of the leading axle commonly experiences a braking moment in a curve which promotes faster crack propagation rates due to hydraulic mechanisms (Kalousek [2005]). Zone 2 (flange and flange root) RCF cracks are less common than RCF cracks in zone 1. Zone 2 RCF cracks are formed by contact between the flange or flange root and the gauge corner of the rail. For a leading axle, this contact imposes a tractive force that tends to close the cracks and making crack propagation aided by hydraulic mechanisms unlikely. Zone 2 cracks are commonly oriented some $30 - 60$ degrees towards the wheel axis (Deuce [2007] and Stone [2004]). Zone 3 (centre of tread) RCF cracks are caused by braking (and traction) on tangent track. RCF cracks at zone 3 are mainly oriented parallel to the wheel axis although there is some scatter in their orientation, see Figure 3.4.

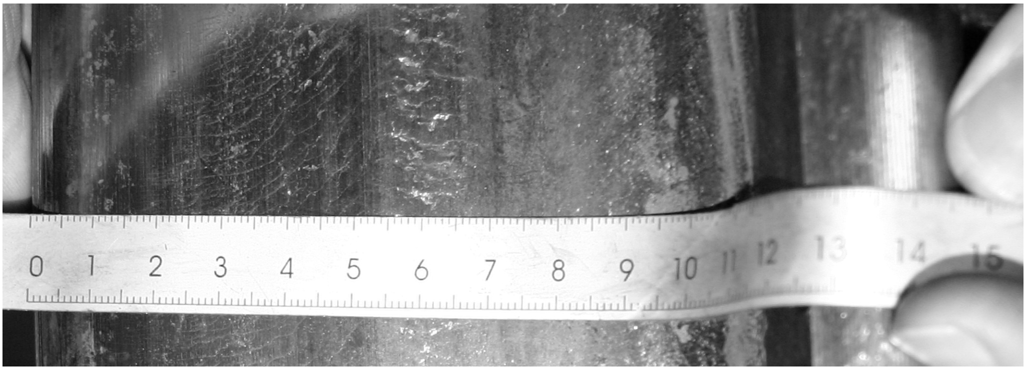

Figure 3.4: *RCF on a locomotive wheel. Zone 1 RCF cracks are seen approximately between 2 to 5 centimetres from the rim face (to the left) and zone 3 RCF cracks between 5 to 7 centimetres. Image courtesy of Anders Ekberg.*

Thermal cracks are caused by heating and subsequent cooling of the wheel. Heating of the wheel can be caused by e.g. tread braking or large-scale wheel slip/sliding. Thermal cracks are formed by the material being plastically deformed due to restrained thermal expansion. When the surface of the wheel subsequently cools, tensile residual stresses are induced, which may cause cracking (Ekberg [2009]). Thermal damage is often (but not always) associated with martensite formation. For martensite to form, temperatures have to have been sufficiently high for austenite to form (i.e. over 700°C) followed by rapid cooling. The martensite and the surrounding heat affected zone may act as initiation areas for fatigue cracks (Ekberg and Kabo [2005]). A milder form of thermal damage is the formation of ”brick” or ”crocodile skin” patterns. Thermal cracks and thermal effects are not considered in the current thesis. The interested reader is referred to Caprioli [2014] and references therein.

3.2 Wear

3.2.1 Wear processes

The broadest definition of wear is the loss (or displacement) of material from a contacting surface (Nilsson [2005]). This broad definition would include RCF as a wear mechanism in cases where RCF leads to spalling. Wear is defined by Johnson [1989] as a steady removal of material from the surface in the form of relatively small particles. Lewis, Dwyer-Joyce, et al. [2010] classify a ratcheting process together with subsequent material removal as a wear phenomenon. Regardless of the exact definition it is clear that RCF and wear are closely related phenomena.

Wear mechanisms for sliding contacts

Contact conditions (e.g. contact pressure and sliding velocity), the (potential) presence of debris, and the material properties of the contacting surfaces, govern which wear process will take place.

Oxidative wear is a wear process where a oxide layer of the material is detached from the surface (Lewis and Olofsson [2009]). Once the oxide has broken off, a new oxide layer starts forming, which will in time be broken away. Oxidative wear takes place under low contact pressures. Wear rates are generally low for oxidative wear.

Adhesive wear is a wear process where contact between surfaces occurs at discrete points corresponding to microscopic surface asperities (Lewis and Olofsson [2009]). When the surfaces move relative to each other, the material is broken away at discrete points either by brittle or ductile fracture. After the material at the original points of contact has broken, contact will occur at new surface asperities.

Abrasive wear is a wear process where damage to a surface is caused by a harder surface or by hard particles (Lewis and Olofsson [2009]). The harder surface/particle acts as a “plough” whereby grooves are formed on the softer surface. If the wear damage to a softer surface is caused by asperities on the harder surface it is referred to as two-body abrasive wear. If hard particles are trapped between the surfaces it is referred to as three-body abrasive.

Delamination wear is a process where cracks nucleate at the plastically deformed surface layer. These cracks propagate parallel to the surface and may merge with other cracks. Eventually material detaches in the form of thin flake-like sheets of wear debris (Suh [1973]).

Thermal wear processes are caused by frictional heating of the surfaces (Lewis and Olofsson [2009]). The heating of the surfaces leads to softening or even melting of the material. The heated material can thereafter be displaced as a viscous fluid.

Classification of wear

Wear is often classified into regimes differentiated by sudden jumps in wear rates. Commonly wear is divided into *mild*, *severe* or *catastrophic* regimes. Mild wear is usually associated with oxidative wear. Severe wear is commonly associated with adhesive or thermal wear mechanisms (Lewis and Olofsson [2009]) and with delamination wear (Lewis, Dwyer-Joyce, et al. [2010]). The wear rate may be pushed into the catastrophic wear regime e.g. by increasing temperatures at the contact and subsequent thermal softening.

The transition between mild and severe wear has been linked by Beagley [1976], with the aid of shakedown diagrams, to the yield strength in shear of the material when the friction is low (below 0.3) and to the fracture strength in shear for high friction cases. The transitions between mild and severe wear have also been shown to correlate with a transition from partial slip to full slip conditions, see Lewis and Dwyer-Joyce [2004] and Lewis, Dwyer-Joyce, et al. [2010].

3.2.2 Wear of rails

Wear of rails in Sweden is quantified by two measures, vertical and horizontal wear (Banverket [1998]). Vertical wear is defined as the vertical difference between an unworn rail and a worn rail at the centreline of the rail. Horizontal wear is defined as horizontal difference between a worn and a nominal rail at a height of 14 millimetres below the top of the head of the worn rail. Examples of worn high rail profiles are presented in Figure 3.5.

A field study by Olofsson and Telliskivi [2003] showed that the measured wear rate of the gauge face (approx. horizontal wear) could be ten times greater than for the top of the rail (vertical wear). The wear of the gauge face was classified as severe whereas the wear of the top of rail was classified as mild. In Lewis and Olofsson [2004] mechanical contact conditions derived from GENSYS simulations are linked to the wear regimes. Mild to severe wear is expected for contacts between the top of rail and the wheel tread whereas severe to catastrophic wear is expected for contacts between the rail gauge and wheel flange.

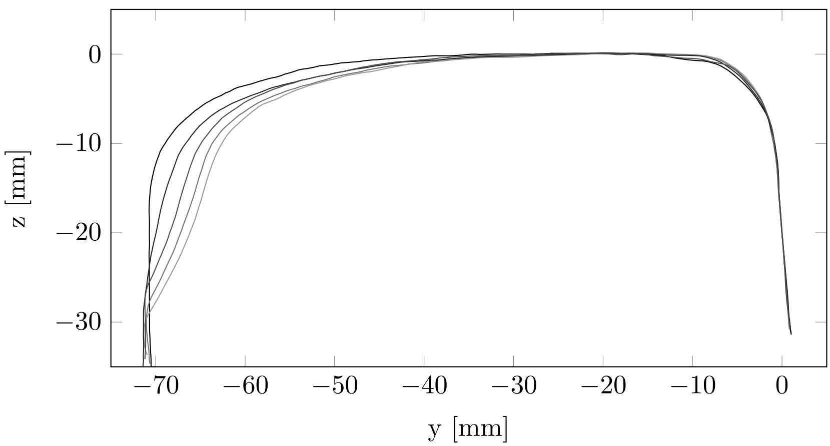

Figure 3.5: *Examples of worn high rail profiles. Note that the profiles are aligned at the field side of the rails.*

3.2.3 Wear of wheels

Currently there are a number of measures which are employed in describing a worn wheel profile as shown in Figure 3.6. There are three commonly used measures of the flange geometry: flange height S_h, flange thickness S_d and flange gradient qR. Hollow wear of the tread is defined by H which is the difference in radius between the smallest radius of the tread (close to the running band) and the largest radius close to the field side. Examples of worn wheel profiles are presented in Figure 3.7.

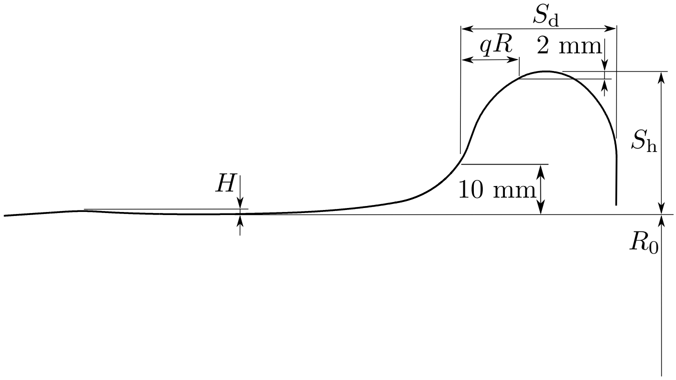

Figure 3.6: *Measures of a worn wheel that are currently employed in maintanence/safety decisions.*

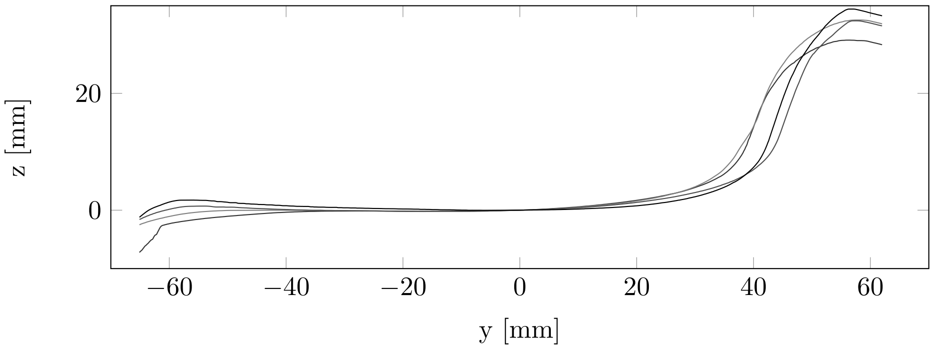

Figure 3.7: *Examples of worn wheel profiles. Profiles measured by Björn Pålsson, see Pålsson and Nielsen [2012] for details.*

4 Numerical investigations

4.1 Wheel/rail contact modelling

The theory of elastic contact by Hertz [1882] is still a commonly used and valuable tool. Setting out from two bodies which come in contact with each other, the origin is set as the point where the first contact occurs. If both bodies are approximated by quadratic functions close to the origin and brought into contact, then the contact area is elliptical. The pressure distribution on the elliptic area, C, with semi-axes a and b is presumed to be described by

$$p(x,\, y) = p_0\sqrt{1 - \left(\frac{x}{a}\right)^2 - \left(\frac{y}{b}\right)^2}, \qquad (x, y) \in C \tag{4.1}$$

where p_0 is the maximum pressure, and x and y coordinates within the elliptic area.

The presumptions that need to be fulfilled for the Hertz theory of contact to be valid and their consequences can be summarised as:

- linear elastic materials implying small strains;
- contacting bodies assumed to be half spaces i.e. the size of the contact area (a and b) is much smaller than dimensions and radii of the contacting bodies, which implies that the contact is non-conformal;
- constant curvature of the contacting bodies in the vicinity of the contact;
- smooth surfaces of the contacting bodies;
- frictionless contact or quasi-identity (see Kalker [1990]) is required to decouple the normal contact problem from the tangential contact problem.

When a wheel in rolling contact is exerting traction, some creep will occur. This was shown by Carter [1926] for a rolling cylinder. It was further shown that an area at the leading edge of the wheel contact area has no relative motion against the rail contact area, i.e. the areas will stick. For the trailing edge of the contact the bodies slide relative to each other, i.e there will be slip between the contacting bodies. The slip portion of the contact area increases as the creep increases until full slip is obtained. At full slip the tractive force can be presumed to be limited by Coulomb's law (normal force multiplied with the coefficient of friction). An example of how stick and slip regions of the contact area evolve with increasing tractive force is given in Figure 4.1.

At the wheel/rail contact where both longitudinal, lateral and spin creep is present the situation becomes more complex. Kalker has proposed several theories from "exact" solutions with the so-called complete theory of rolling contact to approximate solutions with the linear and simplified theories, see Kalker [1979, 1991]. The complete theory with its implementation CONTACT has the constitutive relation derived from the theory of elasticity (thus called an "exact" theory) with the simplifications of half-space assumption and Coulomb friction. The simplified theory and its implementation FASTSIM (Kalker [1982]) is based on the assumptions that the displacement of the surface is proportional to the traction (i.e. can be considered as a set of elastic springs which displace independently), and that Coulomb friction is occurring. FASTSIM is commonly used in railway multibody

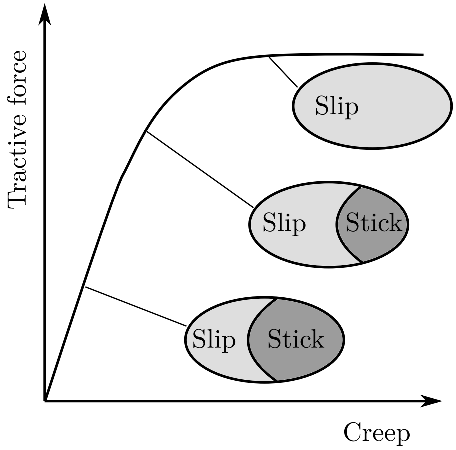

Figure 4.1: *Traction curve and the evolution of stick and slip regions of the contact area for increasing creepage.*

simulation packages due to the low computational cost. The accuracy of FASTSIM is adequate for many cases when compared to CONTACT, see Vollebregt, Iwnicki, et al. [2012].

In cases of conformal contact the half-space assumption is generally not valid. For such conformal contacts a method is presented by Li [2002] where a quarter-space assumption is employed. Differences in results between half-space and quarter-space assumptions for conformal contacts are presented by Vollebregt and Segal [2014]. The contact area is found to be some 30–35% smaller with a quarter-space assumption. Contact pressures increase correspondingly.

All of the wheel/rail contact theories that have been mentioned so far rely on linear elastic material models. To account for plastic deformations, mainly finite element (FE) analyses have been performed. Telliskivi and Olofsson [2001] have compared solutions of wheel/rail contact for elastic-plastic finite element analysis, CONTACT and a Hertzian method. It is shown that for gauge corner contact the FE solution produces a considerably larger contact area than CONTACT and Hertz solution. Consequently, the maximum contact pressure is considerably smaller for the FE solution. For contact between the crown of the rail and the tread of the wheel the differences between the three methods were found to be much smaller. FE-analysis of such contacts have been presented by Zhao and Li [2015]. It is shown how the contact area becomes larger with an elastic-plastic material response than with an elastic material response. Moreover, the contact area becomes more egg shaped when plastic effects are considered. Generally for FE-analyses of wheel/rail contact, surface penetration has to be controlled, cf. Kabo et al. [2010].

4.2 Multibody dynamics simulations

GENSYS is a multibody dynamics simulation package specialised on train/track dynamics (GENSYS [2010, 2014][1]). Quasi-static, modal, frequency-response and time-domain analyses can be performed. In this thesis mainly time-domain analyses were performed (sometimes with an initial quasi-static analysis to serve as an input to a subsequent time-domain analysis). The simulation package also includes supporting programs, e.g. for the generation of wheel/rail geometric functions and generation of track irregularity input files from measured irregularities. The track irregularity input files used in this thesis were however generated by in-house Matlab scripts. Furthermore, post-processing of results was performed in MATLAB [2011].

In **Papers A** to **D**, wheel/rail creep forces were determined by a lookup table calculated by FASTSIM (Kalker [1982]). In the employed GENSYS contact algorithm there can be up to three contact points in simultaneous contact.

4.3 Vehicles included in the study

4.3.1 Freight wagon with Y25 bogies

The freight wagon is modelled after a steel ingot transport wagon. The maximum axle load is 25 tons and the maximum speed when fully loaded is 100 km/h. The bogies are modified Y25 bogies (Y25-TTV) and the main parts are (see also Figure 4.2):

1. Bogie frame
2. Centre-pivot – Transfers the main part of the loads from the carbody to the bogie. The centre-pivot can be regarded as a spherical plain bearing which enables rotation in all directions between the bogie and carbody.
3. Side bearer – Carries some of the load from the car body. Increases the stability of the vehicle through increased damping in the longitudinal direction. Furthermore side bearers reduce carbody roll.
4. Primary suspension – Load dependent vertical damping is provided by the so called Lenoir link.
5. Wheelset.

See Table 4.1 for additional properties.

The numerical model was originally developed and verified by Jendel [1997]. Since then the model has been modified to take advantage of new functionalities of the simulation package GENSYS. The freight wagon model is employed in **Paper A**, **Paper B**, **Paper C** and **Paper D**.

[1] Release 1009 was used in **Papers A** to **C**, and release 1410 in **Paper D**.

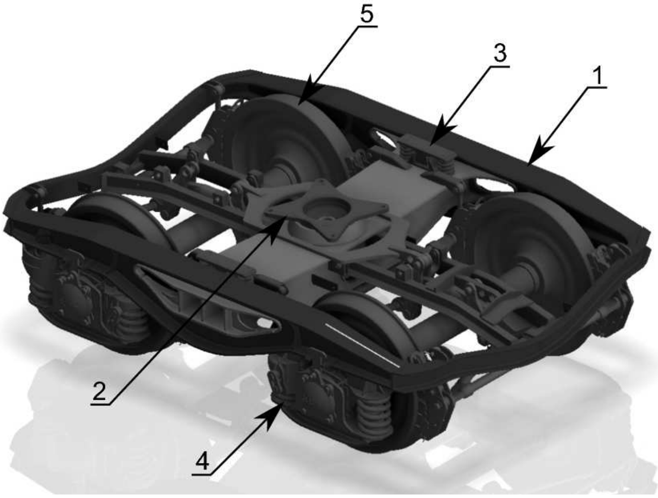

Figure 4.2: *Y25-bogie of the freight wagon. See text for an explanation of the parts (picture courtesy of Igor Antolovic at Kockums Industrier AB).*

Table 4.1: Vehicle properties.

	Iron ore wagon	Freight wagon	Generic locomotive
Designation	Kockums Industrier Fammoorr^{050}	Kockums Industrier Smmnps^{951}	GENSYS
Length between centre line of couplers	10 300 mm	14 240 mm	N/A
Bogie type	three-piece	Y25-TTV	N/A
Bogie c/c distance	6 744 mm	9 200 mm	13 000 mm
Axle bogie distance	1 778 mm	1 800 mm	3 000 mm
Wheel diameter	915 mm	920 mm	1 000 mm
Total height	3 640 mm	1 800 mm	N/A
Tare weight	21.6 tons	20.3 tons	total 80 tons
Load capacity	102 tons	79.7 tons	

4.3.2 Iron ore wagon

The iron ore wagon is a specialised wagon for the Iron Ore Line in northern Sweden. The maximum axle load is 30 tonnes. The maximum speed is 70 km/h at tare weight and 60 km/h at laden weight. The iron ore wagon has the three-piece bogies M976 Motion Control® by Amsted Rails. The main parts of the three-piece bogie are (following numbering in Figure 4.3):

1. Side frame – Connected to the bolster (2) with the coil spring assembly (5) and to the wheelset (7) with the adapter (6).
2. Bolster – The central plate on the bolster connects the bogie to the carbody.
3. Side bearer – Carries some of the load from the car body. Increases the stability of the vehicle due to increased damping in the longitudinal direction.
4. Friction wedge – Wedge between bolster and side frame which by friction provides damping.
5. Coil spring assembly – The main suspension of the bogie.
6. Adapter – Connects the wheelset (via a bearing) with the side frame and provides an elastic coupling in lateral and longitudinal directions.
7. Wheelset.

See Table 4.1 for additional properties.

The numerical model of the vehicle was developed by Bogojević, Dirks, et al. [2011] and Bogojević, Jönsson, and Stichel [2011]. The iron ore wagon model is used in **Paper A**.

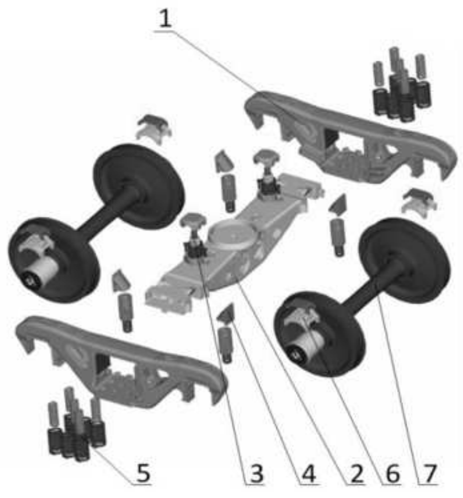

Figure 4.3: *Assembly of a three-piece bogie used in the iron ore wagon. See text for a description of the numbered parts. From Bogojević, Dirks, et al. [2011].*

4.3.3 Iron ore locomotive

The iron ore (IORE) locomotive is not employed in any simulations reported in this thesis but plays a central role in **Paper E**. A locomotive section has two three-axle bogies (Co-Co configuration, see Figure 4.4) and an axle load of 30 tons (total weight of 180 tons per locomotive section), see Bombardier [2008]. The starting tractive effort is 600 kN. These locomotives are always used in pairs which mean that each train has two coupled locomotive sections. The total length of a locomotive section is almost 23 metres, the bogie has a wheelbase of 1.92 metres and the bogie centre distance is 12.9 metres. The locomotives have regenerative braking which is employed in descents to recover energy. Commonly regenerative braking is employed to brake the entire train of 68 wagons, corresponding to a train weight of more than 8000 tonnes.

Figure 4.4: *IORE locomotive.*

4.4 Description of the track model

In the multibody simulations presented in **Paper A** to **Paper D** the vehicle model is connected via the wheel/rail interface to a track structure which in turn is connected to the ground. Each wheelset is coupled to a moving track model. The track model in Figure 4.5 mimics the properties of a track section on a Swedish main line with UIC60 rails and concrete sleepers. Spring stiffness, damping coefficients, and masses can be found in the documentation of GENSYS [2014]. For details on the track section and on the measurement of track properties see Chaar [2007]. It should be noted that the spring connecting the rail to the track ($k_{\mathrm{z,rt}}$) has a stiffness that varies along the track to mimic the variation in the rail stiffness due to sleeper spacing.

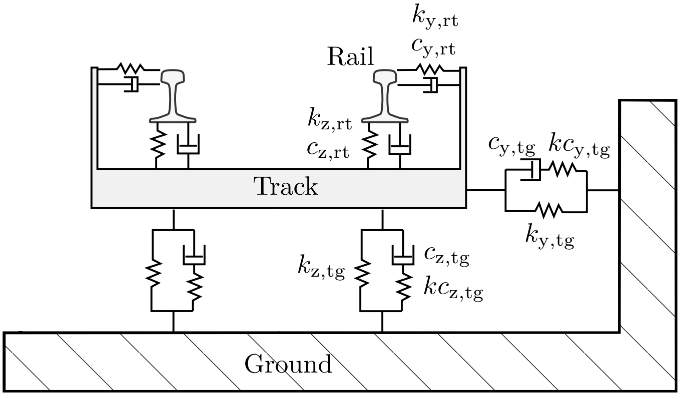

Figure 4.5: *Track model with designations of springs and dampers between parts.*

4.5 Models for prediction of RCF and wear

4.5.1 RCF prediction

Shakedown map based analysis

A prediction model for *surface* initiated RCF is presented by Ekberg, Kabo, and Andersson [2002]. The RCF prediction model sets out from the shakedown map by Johnson [1989] where surface initiated RCF is linked to the plastic deformation of the contact surface. Following Hertz theory the maximum pressure (p_0) from Eq. 4.1 can be expressed as (see e.g. Johnson [1985])

$$p_0 = \frac{3}{2}\frac{F_{\mathrm{z}}}{\pi ab} \tag{4.2}$$

where F_{z} is the normal force. A maximum inter-facial shear stress at the contact area can, for full slip conditions, be expressed as

$$q_0 = fp_0 \tag{4.3}$$

where $f = \sqrt{F_{\mathrm{x}}^2 + F_{\mathrm{y}}^2}/\sqrt{F_{\mathrm{z}}^2}$ is the traction coefficient with the tangential longitudinal F_{x} and lateral F_{y} wheel/rail contact forces (coordinate system is shown in Figure 2.1). Ratcheting at the contact surface is assumed to occur if the cyclic yield stress in shear (k) is exceeded, i.e.

$$q_0 > k. \tag{4.4}$$

In this thesis k is taken as 300 MPa. Combining Eq. 4.2–4.4 gives

$$f - \frac{2\pi abk}{3F_{\mathrm{z}}} > 0 \tag{4.5}$$

from where it is clear that plastic deformation will occur only if the traction coefficient is greater than the cyclic yield limit in shear divided by the peak normal pressure. Ekberg, Kabo, and Andersson [2002] formulate an RCF index as:

$$FI_{\text{surf}} \equiv f - \frac{2\pi abk}{3F_{\text{z}}}. \tag{4.6}$$

Eq. 4.6 quantifies the horizontal distance between the utilised friction coefficient and the cyclic yield stress in shear divided by the maximum normal contact stress in the shakedown map (see Figure 4.6). Ratcheting is assumed to occur if $FI_{\text{surf}} > 0$.

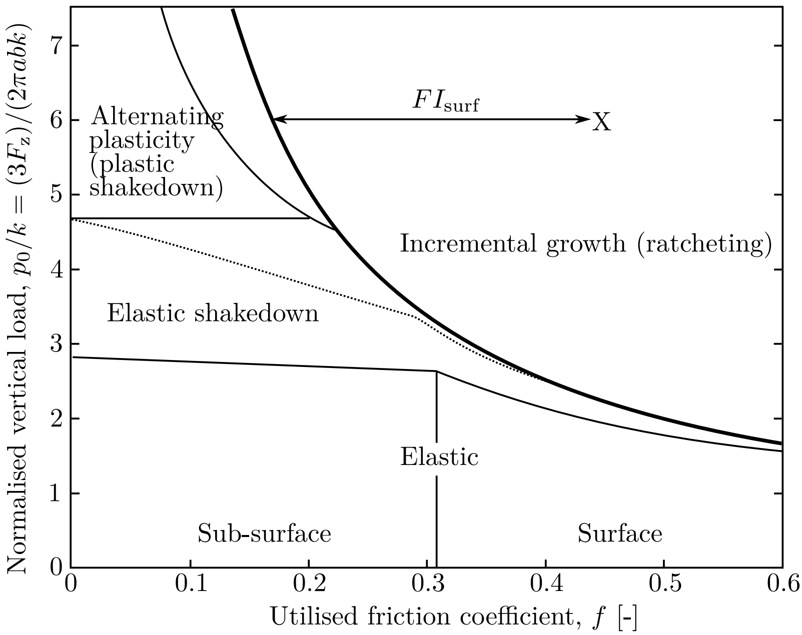

Figure 4.6: *Definition of FI_{surf} in the shakedown map (after Ekberg, Kabo, and Andersson [2002]).*

Comparisons made by Kabo et al. [2010] of predicted FI_{surf} values and experimentally found fatigue lives (from a full-scale roller rig, a full-scale linear test rig, and a twin-disc machine) indicated a Wöhler-like relationship

$$FI_{\text{surf}} = 1.78(N_{\text{f}})^{-0.25} \tag{4.7}$$

where N_{f} is the fatigue life to RCF crack initiation. Equation 4.7 can be reformulated to quantify (surface initiated) RCF damage per cycle

$$D \equiv \frac{1}{N_{\text{f}}} = \frac{(FI_{\text{surf}})^4}{10} \quad \forall\, FI_{\text{surf}} \geq 0. \tag{4.8}$$

FI_{surf} according to Eq. 4.6 is used in all appended papers whereas damage evaluation according to Eq. 4.8 is used in **Paper A**.

$T\gamma$ based analysis

A model predicting RCF damage has been proposed by Burstow [2004]. Here an index $T\gamma$ is calculated as

$$T\gamma = F_{\mathrm{x}}\gamma_{\mathrm{x}} + F_{\mathrm{y}}\gamma_{\mathrm{y}} \tag{4.9}$$

where γ_{x} and γ_{y} are creepages in longitudinal and lateral directions. Note that spin creep is not explicitly considered when evaluating $T\gamma$.

The RCF damage function is derived by Burstow [2004] by comparing actual RCF damage locations on rails to predictions featuring multibody simulations at four different locations in the UK. The studied curves have radii between 400 and 3000 metres. The traffic at the locations were mainly electric multiple units (i.e. commuter trains). The function relating RCF damage to $T\gamma$ is presented in Figure 4.7. It can be seen that the damage function has a maximum value for $T\gamma = 65\,\mathrm{N}$. Thereafter the damage function decreases to negative damage magnitudes. This can be interpreted as wear becoming the dominant damage mechanism and RCF cracks are truncated as shown in Figure 4.8. An accumulated damage of unity is presumed to correspond to a crack with a surface length of 2 millimetres (Burstow [2004]).

The $T\gamma$ model according to Eq. 4.9 and Figure 4.7 is employed in **Paper A** and **Paper B**.

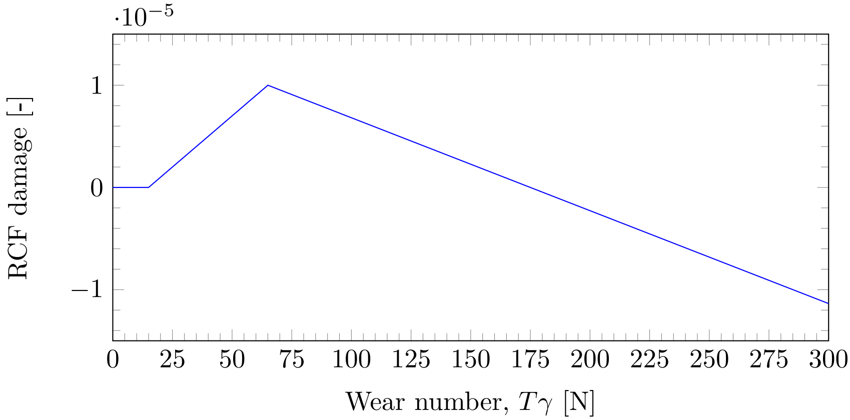

Figure 4.7: *Wear number based damage function following Burstow [2004].*

4.5.2 Wear prediction

Archard's wear equation

Archard [1953] proposed an equation relating the wear rate to the load, the radius of a single surface asperity in contact and a probability factor. Later the hardness of the material was included in the wear model. The volume of the worn-off material, V, can be

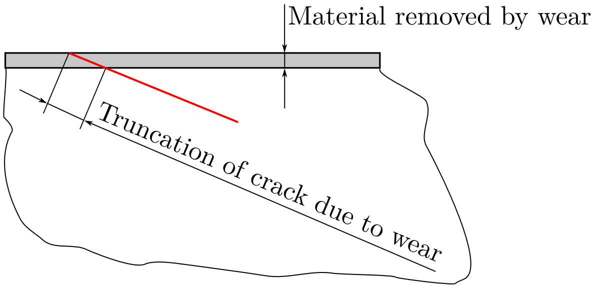

Figure 4.8: *Truncation of a crack due to wear.*

predicted as

$$V = \mathrm{K}\frac{Ps}{H} \tag{4.10}$$

where K is a non-dimensional wear coefficient, P [N] is the normal load, s [m] is the sliding distance and H [N/m^2] is the hardness of the material. The rate of wear is obtained by replacing the sliding distance with the sliding velocity in Eq. 4.10. Calculation of wear rates according to Eq. 4.10 are not considered in the current thesis.

Wear models based on dissipated energy

Energy dissipated in the contact patch has been employed as a measure to identify wear regimes and wear rates. It should be remembered that especially the transition in wear regime between severe and catastrophic wear is dependent on the steel grade (Lewis, Dwyer-Joyce, et al. [2010]). Simulations of wheel wear by Pombo et al. [2011] show that only small variations are found in results between global and local wheel/rail contact models and wear functions. A global wear function presented in Pearce and Sherratt [1991] is classified by Pombo et al. [2011] into the different wear regimes as: mild wear for $T\gamma < 100$ N, severe wear for $100 \leq T\gamma < 200$ N and catastrophic wear for $T\gamma \geq 200$ N. This classification is used in **Paper C** and **Paper D**.

4.6 Design of experiments

In **Paper C** and **Paper D**, a design of experiments method is employed to analyse the influence of the involved parameters. In **Paper C** a hollow wheel profile is parametrised whereas in **Paper D** both the gauge corner of the rail and flange root of the wheel are parametrised. Also some track geometry features are here considered as parameters. In both papers nearly orthogonal and space-filling Latin hypercube (NOLH) sampling is used to create different scenarios which are subsequently employed in multibody simulations. The results of multibody simulations featuring these scenarios provide degradation indices which are subjected to regression analysis to derive meta-models.

4.6.1 Nearly orthogonal and space-filling Latin hypercubes

Cioppa and Lucas [2007] describe a method to produce design matrices which are both space-filling and (nearly) orthogonal, so-called nearly orthogonal and space-filling Latin hypercubes (NOLH). By slightly relaxing the orthogonality requirement the space-filling properties of the designs are improved. The advantage with a space-filling design is that the design points are scattered throughout the whole experimental region. Orthogonality implies that the different input parameters (columns of a design matrix) are uncorrelated. This is a desirable feature since it facilitates the decision of whether a parameter should be kept in the meta-model. It further makes it easier to separate the contribution of each parameter to a meta-model fit. An example of the distribution of design points over a design space is shown in Figure 4.9. A further introduction to designing simulation experiments and an outline of the difference to "classic" design of experiments can be found in Kleijnen et al. [2005].

4.6.2 Regression analysis

A meta-model with linear, quadratic and bilinear terms can be expressed as

$$y(\mathbf{x}_r) = \beta_0 + \sum_{s=1}^{u} \beta_s x_s + \sum_{s=u+1}^{2u} \beta_s x_s^2 + \sum_{s=1}^{u-1} \sum_{t>s}^{u} \beta_{s,\,t} x_s x_t \tag{4.11}$$

where $y(\mathbf{x}_r)$ is the response for the r:th scenario for the design points $\mathbf{x}_r = (x_1,\, x_2, \ldots, x_{p-1})$ and β are the regression parameters. The total number of parameters of the above meta-model is

$$p = 1 + u + u + \binom{u}{2} = 1 + 2u + \frac{u(u-1)}{2} \tag{4.12}$$

where $\binom{u}{2}$ is the binomial coefficient[2]. Non-significant terms are discarded, which means that not all of the input parameters are necessarily present in the final meta-model.

The regression coefficients are estimated by linear least squares fitting where the residual sum-of-squares are minimised. If the response and regression parameters are gathered in vectors ($\mathbf{y}$ and $\boldsymbol{\beta}$) and the design points for the scenarios are collected into a matrix ($\mathbf{X}$), then the residual sum-of-squares can be written

$$\mathrm{RSS}(\boldsymbol{\beta}) = (\mathbf{y} - \mathbf{X}\boldsymbol{\beta})^T(\mathbf{y} - \mathbf{X}\boldsymbol{\beta}). \tag{4.13}$$

Differentiation with respect to β and setting the derivative to zero yields

$$\mathbf{X}^T(\mathbf{y} - \mathbf{X}\boldsymbol{\beta}) = 0. \tag{4.14}$$

The optimal regression parameters in a least squares sense can thus be obtained from

$$\hat{\boldsymbol{\beta}} = (\mathbf{X}^T\mathbf{X})^{-1}\mathbf{X}^T\mathbf{y}. \tag{4.15}$$

With $\hat{\boldsymbol{\beta}}$ established, the response can be evaluated as

$$\hat{\mathbf{y}} = \mathbf{X}\hat{\boldsymbol{\beta}} \tag{4.16}$$

[2] $\binom{n}{k} = \dfrac{n!}{k!(n-k)!}$

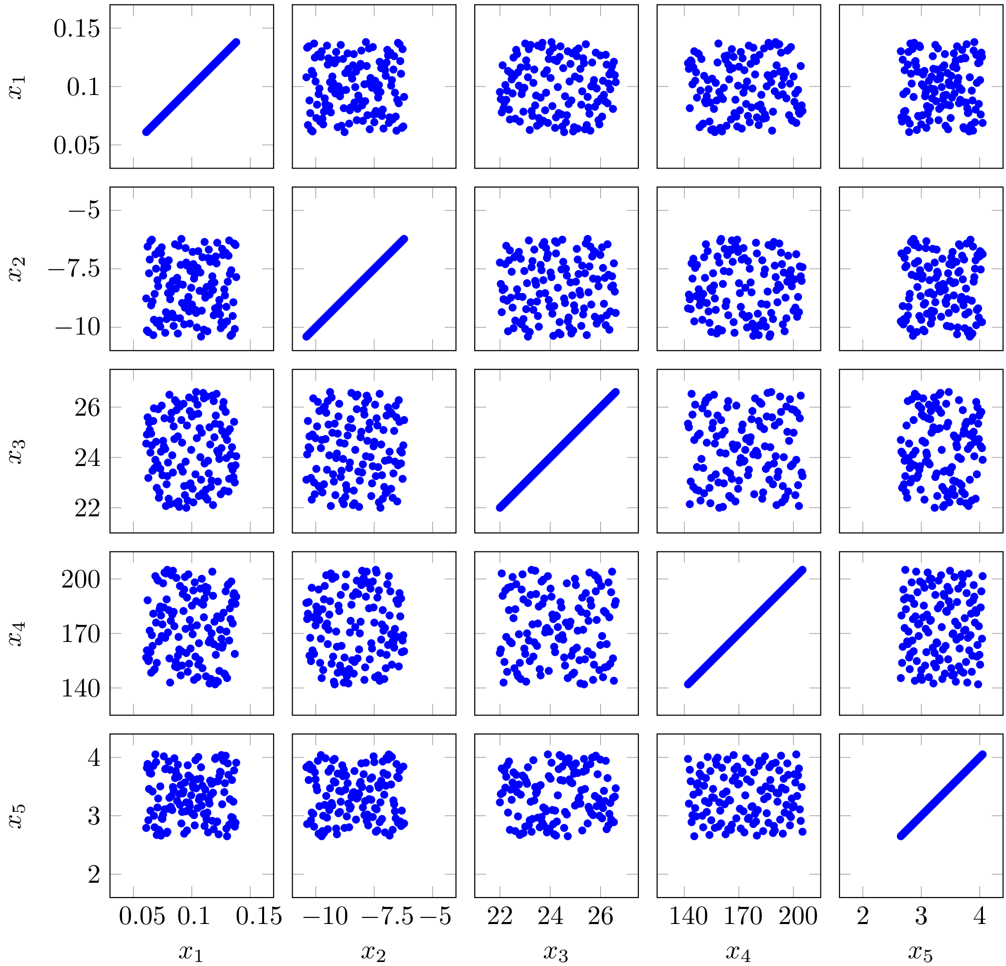

Figure 4.9: *Scatter plots between the five first parameters (x_1 to x_5) of the design matrix used in* ***Paper D****.*

4.6.3 Fitting of conics

In **Paper D** the coefficients of the general second degree equation for a parabolic solution (as described below, see Eq. 5.1) are identified for measured wheel and rail profiles. The coefficients are identified with a direct method of fitting a specific type of conic section to scattered data presented in Harker, O'Leary, and Zsombor-Murray [2008]. This method is computationally effective.

5 Summary of appended papers

In this section brief outlines of the appended papers are given. The main geometric parameters that are considered in each paper are illustrated in Table 5.1.

Table 5.1: Scope of the appended papers.

	Paper A	**Paper B**	**Paper C**	**Paper D**	**Paper E**
Track geometry	✓	✓	✓	✓	✓
Track irregularities	✓	✓	(✓)		✓
Wheel profile geometry			✓	✓	✓
Rail profile geometry				✓	✓

Paper A is a study of how lateral track irregularities influence track shift forces (see Section 2.2.3) and evaluated RCF indices (see Section 4.5.1). Measured track geometry including irregularities from twelve curves at the Iron Ore Line in Sweden are employed in multibody dynamics simulations. The curve radii range between 390 to 1655 metres. Two different vehicle models (an iron ore wagon with three-piece bogies and a freight wagon with Y25 bogies) are employed in the simulations. Measured lateral irregularities are scaled to mimic different states of a laterally deteriorated track geometry. The wheel/rail friction coefficient is varied between 0.3 and 0.6. It is shown that standard deviations of lateral irregularities and track shift forces have a roughly linear relationship. Furthermore, the track shift forces are not significantly influenced by a variation of the wheel/rail friction coefficient. Two RCF indices are employed in the study, a shakedown map based criterion (Eq. 4.6) and a wear number based criterion (Eq. 4.9 together with Figure 4.7). At sharp curves the damage shifts from pure wear for low levels of lateral irregularities to a mix of wear and RCF for higher levels of lateral irregularities. For shallow curves the length of rail affected by RCF increases for increasing levels of lateral irregularities. An increase of the friction coefficient generally leads to higher RCF damage magnitudes.

Paper B is a continuation of the previous paper. Both single lateral irregularities and lateral irregularities generated from power spectral densities (PSD) are employed in multibody simulations featuring a freight wagon with Y25 bogies. Single lateral irregularities are applied to a straight track to study which irregularity amplitude and length that will cause RCF. For curves between 500 and 3000 metres in radius, generated random lateral irregularities are applied. Similar results are obtained as in **Paper A** i.e. for shallow curves (radii larger than 1250 metres) the length of track affected by RCF increases with increasing levels of lateral irregularities. The 95th percentile magnitude of FI_{surf} is not significantly affected by an increase in the level of lateral irregularities for curves with a radii of 2000 metres or less. Furthermore, lateral irregularities in wavelength spans (2–10 metres, 10–25 metres and 10–50 metres) are amplified and employed in multibody simulations. For curves larger than 1250 metres it is found that amplification of irregularities in the longer wavelength spans results in the highest increase of RCF index magnitudes (both in terms of length of track affected and the 95th percentile of FI_{surf}). Also a correlation study between predicted tangential wheel forces in the track plane and lateral irregularities (amplitudes of the irregularities, first order derivatives and second order derivatives) is conducted. No significant correlation is found.

Paper C presents a methodology where parameters describing a hollow worn wheel profile can be linked to degradation indices. The wheel profile is parametrised with segments of ellipses and circles as shown in Figure 5.1. In short, the hollow worn tread is approximated by two ellipses which are superposed to the nominal tread of a S1002 wheel profile. Transitions from the ellipses to the nominal wheel profile are made smooth by applying a circular geometries. It should here be noted that the validity of the parametrisation has only been tested for rather a few number of measured wheel profiles. In addition to wheel geometry parameters, curve radii and cant deficiency are included as parameters. Scenarios are created with NOLH sampling, see Section 4.6.1. Wheel profiles and track geometries corresponding to the different scenarios are employed in multibody simulations featuring a freight wagon with Y25 bogies. Median FI_{surf} and $T\gamma$ magnitudes are evaluated from the multibody simulations. These are subsequently subjected to a regression analysis. The end results are meta-models linking wheel profile parameters to degradation index magnitudes.

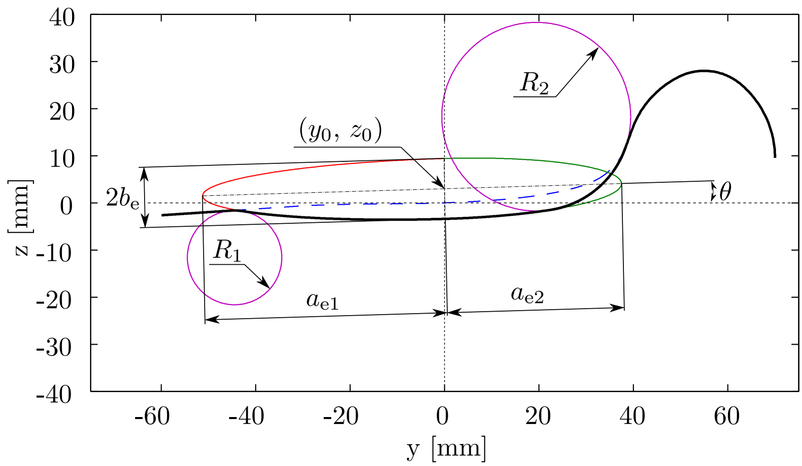

Figure 5.1: *Generation of a single false flange hollow worn profile with geometric shapes from a nominal S1002 wheel profile.*

Paper D employs a similar methodology as presented in **Paper C**. In this paper the gauge corner and flange root geometries are parametrised by fitting a general two-dimensional second order equation (i.e. a conic section)

$$a_i y^2 + b_i yz + c_i z^2 + d_i y + e_i z + f_i = 0 \tag{5.1}$$

where y and z are the lateral and vertical coordinates, respectively; and $i = \{r, w\}$, where r represents the rail and w the wheel. The solutions are forced to become parabolic by prescribing the discriminant $b_i - 4a_ic_i = 0$. They are further normalised so that $a_i + c_i = 1$. The gauge face and the flange face are both approximated by straight lines. Measured wheel and rail profiles are analysed to establish parametric ranges for the geometric parameters. In addition to wheel and rail geometry parameters, also curve radii and cant deficiency are included as parameters. Scenarios are created with NOLH sampling. These are then employed in multibody simulations featuring a freight wagon with Y25 bogies. Median FI_{surf} and $T\gamma$ magnitudes are evaluated and subsequently subjected to a regression analysis. The end results are meta-models linking the parameters to the degradation index magnitudes.

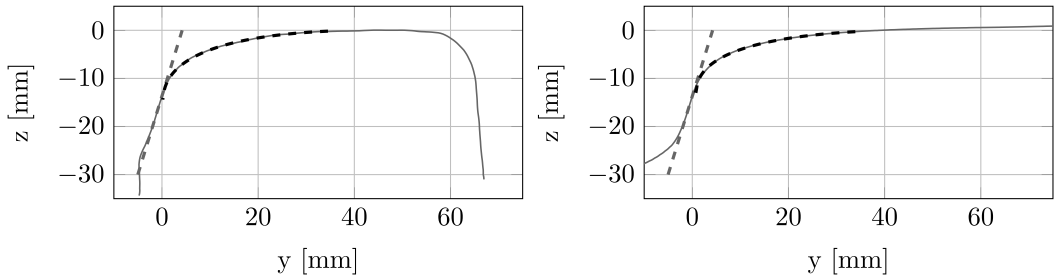

Figure 5.2: *Parametrisation of the gauge corner of the rail profile (left) and flange of the wheel profile (right). The black dashed lines represent the parabolas and the grey dashed lines represent the straight lines.*

Paper E gives an explanation of root causes behind RCF damage found on locomotive wheels operating on the Iron Ore Line in Northern Sweden. It is noted that the highest number of wheel reprofilings due to RCF are made in the last five months of the year. The formation and evolution of RCF are explained in terms of seasonal variations in climate, rail profile geometries and lubrication. The hypothesis is that during the winter months (when most wheels have been reprofiled) crack formation is occurring at a moderate rate. During spring, track based lubrication is turned on and a more humid climate decreases the propencity for crack initiation, but causes initiated cracks to propagate faster. During the summer months the rails are ground, which introduces a profile mismatch. This will increase both the initiation and propagation rates of crack growth. During autumn and winter the profile mismatch is gradually decreasing and the wheels will be subjected to lower stress and damage magnitudes. It is also shown that the operational distance between reprofilings for different locomotive sections can vary as much as by a factor of 2 to 3.

6 Analyses and results

In this section selected results from the appended papers are discussed. Results from the appended papers are tied and in some cases are further explained. Moreover, results from the literature which relate or give further explanation to the discussed topics are highlighted.

6.1 Track geometry and irregularities

As demonstrated in **Paper A** to **D**, the most important factor (of the factors investigated in this thesis) regarding wheel/rail degradation is the curve radius. **Paper A** and **Paper B** show that $FI_{\text{surf}} > 0$ along a greater length of the curve when the curve radius decreases. This is shown in Figure 6.1 where results for the freight wagon with Y25 bogies are presented.

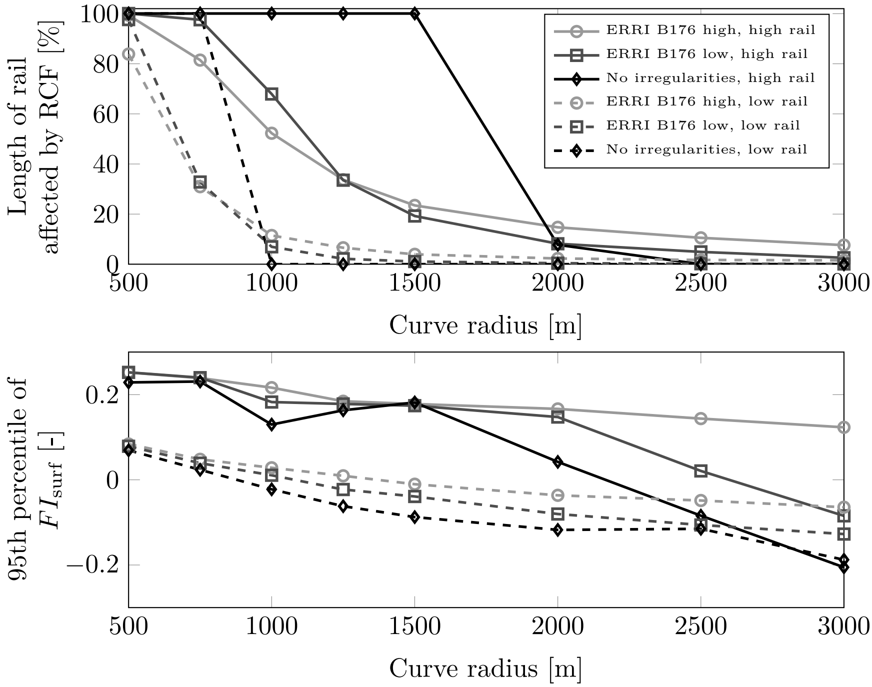

Figure 6.1: *Top: Percentage of rail length with predicted RCF. Bottom: 95th percentile of FI_{surf} over the curve. Results from simulations featuring a freight wagon with Y25 bogies. Figure from* ***Paper B****.*

The high and low level of lateral irregularities in Figure 6.1 are (generated) lateral irregularities according to ERRI [1989] that correspond to standard deviations of about

1.1 mm and 0.65 mm, respectively, in the 3 to 25 metre wavelength span. These standard deviations can be compared to the limits given in Table 2.2.

Also seen in Figure 6.1 is that lateral irregularities influence the portion of the curve where $FI_{\mathrm{surf}} > 0$ differently depending on the curve radius. For curves with a small radius, lateral irregularities decrease the portion of the track affected by RCF (as estimated by FI_{surf}). The opposite is seen for large radius curves where the portion of the curve where $FI_{\mathrm{surf}} > 0$ increases when the level of lateral irregularities are increased. The 95th percentile of FI_{surf} is more influenced by irregularities for larger curve radii than small. This means that for large radius curves RCF defects may initiate at a few large irregularities. A further explanation is given by Figure 6.2 where results are presented for FI_{surf} and $T\gamma$ based RCF damage criteria. For the 438 metre radius curve and no lateral irregularities (Figure 6.2a), FI_{surf} predicts RCF damage for along almost the entire curve whereas the $T\gamma$ based criterion predicts mainly wear. When lateral irregularities are introduced, FI_{surf} damage magnitudes decrease locally along the curve whereas $T\gamma$ based criterion predicts both wear and RCF. The 1578 metre curve in Figure 6.2b corresponds to the curve range for the high rail where a transition from long to short lengths of track affected by RCF is seen in Figure 6.1. For the 1578 metre radius curve an increase of lateral irregularities decreases the length of track with predicted RCF damage. Moreover the lateral position of the contact point towards the flange of the wheel in Figure 6.2b corresponds to the same locations where the largest RCF damage occur. This implies that single large irregularities (causing contact closer towards the flange) may be the cause of head check clusters in curves. Similar conclusions have been drawn in RSSB [2010] where an improvement of lateral track quality is considered as the primary remediation action to reduce RCF for curves more shallow than 1800 metres. Since local variations in lateral track quality may cause RCF, RSSB [2010] recommends a limit on the amplitude of the irregularities rather than a limit on the standard deviation of the lateral irregularities.

Paper C includes an initial example of a meta-model estimating median FI_{surf} magnitudes with lateral track irregularities as a parameter. The meta-model for the inner hollow worn wheel of a freight wagon with Y25 bogies is

$$\begin{aligned}\widehat{FI}_{\mathrm{LI}} =& 0.461 - 6.59\, a_{\mathrm{e1}} + 24.0\, b_{\mathrm{e}} - 10.8\, \theta + \frac{12.8}{R_{\mathrm{c}}}\left(1.0 + 230\, \theta + 4.12\, Lat^3\right) - 0.366\, h_{\mathrm{d}} \\ & - 0.128\, Lat \end{aligned} \tag{6.1}$$

where R_{c} is the curve radius in metres, h_{d} is the cant deficiency in metres and Lat is a scaling factor between 0 (no irregularities) and 1 (high level acc. to ERRI B176) for lateral track irregularities. The scaling factor of the lateral irregularities is included in the meta-model as a negative linear term and as a positive bilinear term together with the curvature of the curve. This is a reflection of the results shown in Figure 6.1 for the low rail (inner wheel). However when only considering the curve radius and the scaling factor of lateral irregularities, the relatively simple response surface (see Figure 6.3a) does not seem to capture the response presented in Figure 6.1a. Instead the part of the meta-model considering only curve radius and lateral irregularities should rather be of the following general type

$$\frac{R_0 - R_{\mathrm{c}}}{R_{\mathrm{c}}^{\eta}}\left(Lat_0 - Lat\right) \tag{6.2}$$

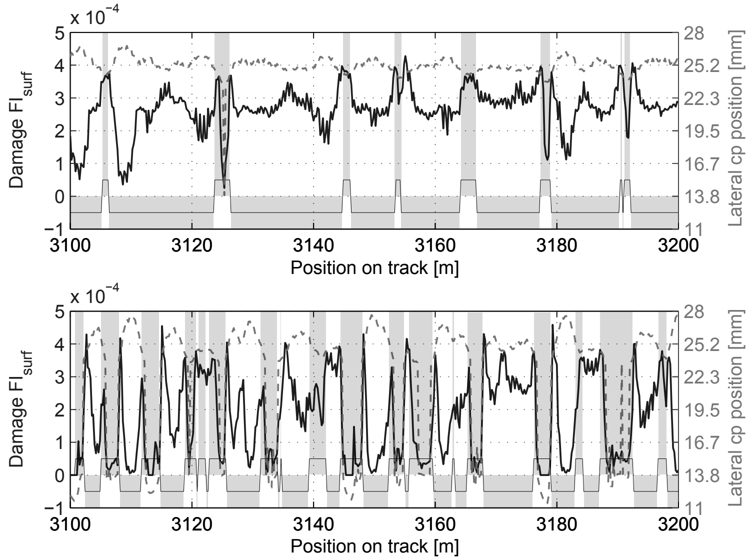

(a) *Simulation featuring a 438 metre radius curve with no lateral irregularities (top) and lateral irregularities with a standard deviation of* 2.94 *mm (bottom).*

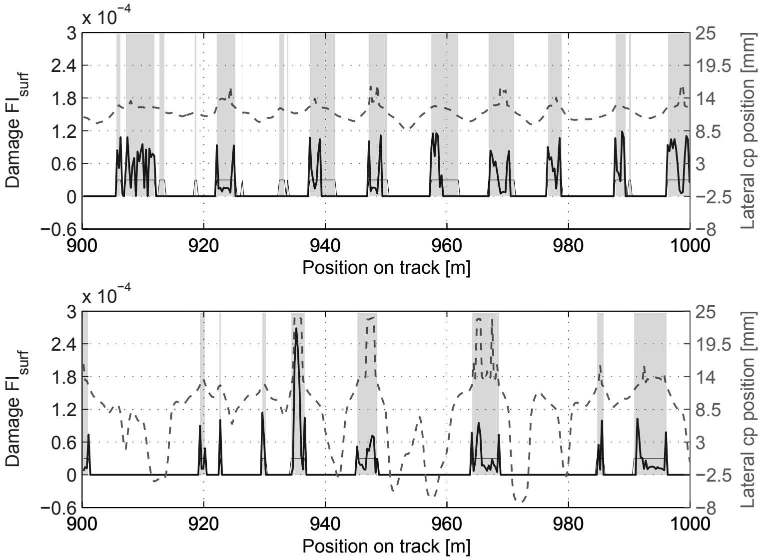

(b) *Simulation featuring a 1578 metre radius curve with no lateral irregularites (top) and lateral irregularities with a standard deviation of* 2.58 *mm (bottom).*

Figure 6.2: *Predicted response of the leading outer wheel (high rail) of a freight wagon with Y25 bogies. RCF damage as quantified by Eq. 4.7 (solid curve, left vertical axis), lateral contact point position on the rail (larger values closer to the gauge corner, dashed curve, right vertical axis) and grey area indicates wheather the* $T\gamma$ *criterion (Eq. 4.9 and Figure 4.7) predicts RCF (positive) or wear (negative). Figures from* ***Paper A****.*

where R_0, Lat_0 and η are constants. Eq. 6.2 creates a twisted response surface as shown in Figure 6.3b. The response following (6.2) decreases with increasing level of lateral irregularities for curves with small radii and increases with increasing level of lateral irregularities for larger curve radii. The drawback with a response surface following Eq. 6.2 is that non-linear regression has to be employed. Cant deficiency, h_{d}, is also included in Eq. 6.1 as a parameter. Increase in the cant deficiency will give lower $\widehat{FI}_{\mathrm{LI}}$ magnitudes. This is an indication that RCF damage can be reduced by introducing some cant deficiency. For the iron ore wagon similar results have been presented by Hossein Nia, Jönsson, and Stichel [2014] where the probability of RCF of inner wheels is reduced by increasing the cant deficiency. However, the benefit was limited to curve radii smaller than 450 metres whereas for curve radii in the 450 to 650 metre range the cant deficiency had no significant effect. RSSB [2010] reports that increasing the cant deficiency for curves between 1000 and 1800 metres in radius may be employed to mitigate RCF. As stated in RSSB [2010], the influence of cant deficiency depends on vehicle parameters such as primary yaw stiffness, suspension arrangement of the vehicle etc. Based the above discussion, it seems that the effect of cant deficiency on wheel and rail degradation can only be determined on a case by case basis.

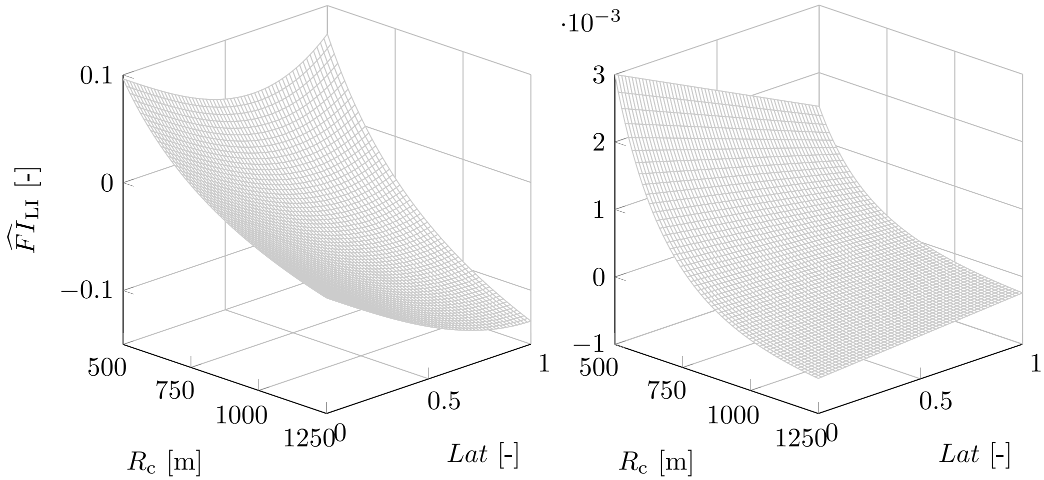

Figure 6.3: *Left: Influence of curve radius (R*c*) and scaling factor of lateral irregularities (Lat) on* $\widehat{FI}_{\mathrm{LI}}$ *following Eq. 6.1 with:* $a_{\mathrm{e1}} = 55\times10^{-3}\,\mathrm{m}$, $b_{\mathrm{e}} = 6\times10^{-3}\,\mathrm{m}$, $\theta = 35\times10^{-3}\,\mathrm{rad}$ *and* $h_{\mathrm{d}} = 0$. *Right: Example of an alternative response surface following (6.2) with* $R_0 = 875\,\mathrm{m}$, $\eta = 2$ *and* $Lat_0 = 2$.

The influence of lateral irregularities on predicted RCF at different wavelengths is also studied in **Paper B**. Lateral irregularities were generated to from power spectral densities in ERRI [1989] corresponding to low and high levels of irregularities. Low level irregularities were amplified to the high level of irregularities in three wavelength spans (2 to 10 metres, 10 to 25 metres and 10 to 50 metres). For curves with a radius of 1250 metres and larger, amplification of lateral irregularities in the two longer wavelength spans increased the length of rail affected by RCF (as defined by $FI_{\mathrm{surf}} > 0$) almost to the same length as found for the high level of lateral irregularities. An amplification in the 2 to 10 metre wavelength span had no significant influence for curves with a radius of 1250 metres and larger. In general, the results for low and high level of irregularities can be seen as bounds within which results for the amplified lateral irregularities fall.

6.2 RCF and wear of wheels

In **Paper E** root causes behind observed wheel damage are sought. **Paper E** sets out from observed seasonal variations of the number of wheel reprofilings and damage patters on Iron ore locomotive wheels. The number of reprofiling of wheels due to RCF damage is found to be larger for the last quarter of the year. This is assumed to be related to a mismatch between wheel and rail profiles since grinding of rail profiles is performed between June to August. The mismatch is believed to increase the contact stress magnitudes which promotes both crack initiation and growth. Over the last quarter of the year the mismatch between rails and wheel profiles decrease due to wear and plastic deformation. After a peak in reprofilings during late autumn/early winter, the new year starts with a relatively low number of reprofilings. When spring comes, the climate becomes more humid and rail lubrication is turned on. This may lead to accelerated crack propagation of wheels reprofiled in autumn assisted by hydraulic mechanisms which leads to a slight peak in reprofilings during spring.

Also shown in **Paper E** is that a change in operational conditions may lead to unforeseen consequences. One such change was finalised in 2011 with the increase from 52 to 68 wagons in a train set. The consequence was an increased number of reprofilings of locomotive wheels due RCF. To reduce the number of reprofilings due to the more severe loading at wheel/rail interface caused by the longer trains, the contact conditions were made less severe with the introduction of an improved low rail profile.

Hollow worn wheels are studied in **Paper C**. For the generated hollow worn wheel profiles, the correlation between measures employed in maintenance (H, qR and S_{d} in Figure 3.6) and resulting FI_{surf} magnitudes were low for both the inner and outer wheel. Somewhat higher correlations were found between the maintenance measures of the wheel and $T\gamma$ magnitudes for the inner wheel for a 500 metre curve radius. However, the correlation becomes lower for larger curve radii. A meta-model based on a parametrisation of the hollow worn part of the wheel profile (see Figure 5.1) improves the correlation significantly. An example of such meta-model has already been presented in Eq. 6.1.

6.3 RCF and wear of rails

In **Paper D** meta-models are derived which estimate degradation index magnitudes for different gauge corner and flange root geometries. The main inputs to the meta-models are coefficients of the general second degree equation (Eq. 5.1), curve radii and cant deficiency. Three types of meta-models are derived:

1. A meta-model predicting whether contact between the wheel profile and gauge corner region as defined in Figure 6.4 occurs. This evaluation is employed as a decision boundary, see Eq. 6.3 below.
2. A meta-model estimating median FI_{surf} magnitudes which is valid when contact occurs at the gauge corner. See Eq. 6.4 below.
3. A meta-model estimating median $T\gamma$ magnitudes which is valid when contact occurs at the gauge corner. See Eq. 6.5 below.

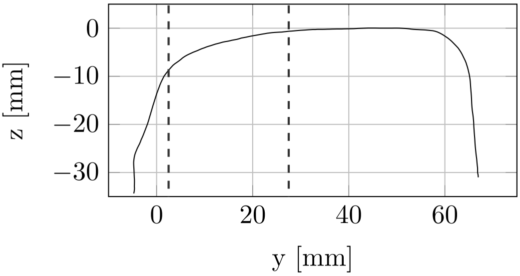

Figure 6.4: *Definition of the gauge corner contact region for the decision boundary in Eq. 6.3. The gauge corner contact region is between lateral coordinates 2.5 and 27.5 mm (represented by the dashed lines) when the rail profile has it's lateral origin at the gauge measuring point (14 mm below top of rail).*

For easier interpretation of the meta-models, Figure 6.5 shows how variations of some coefficients of Eq. 5.1 alter the shape of the gauge corner. An increase of a_{r} leads to a clockwise rotation of the parabola, an increase of d_{r} leads to a lateral scaling of the parabola, an increase of e_{r} leads instead to a vertical scaling and finally an increase of f_{r} leads to a scaling in both directions. Since the wheel profile is parametrised in the same way as the rail profile, the changes to the wheel profile by an alteration of the coefficients are analogous to the rail profile.

The decision boundary presented in **Paper D** is

$$\mathrm{DB} = -0.75 - 11\,a_{\mathrm{r}} - 0.13\,d_{\mathrm{r}} + 6.6 \times 10^{-2} e_{\mathrm{r}} + 19\,a_{\mathrm{w}} + 0.14\,d_{\mathrm{w}} - 3.9\ \times 10^{-2} e_{\mathrm{w}} \quad (6.3)$$

where all coefficients are assumed to be derived for wheel and rail profiles measured in millimetres. If $\mathrm{DB} < 0.5$, it is expected that contact on the rail shoulder will occur. By studying Figure 6.5 it is clear that Eq. 6.3 seems to be a sound decision bound. This can be exemplified by regarding an increase of a_{r} which makes contact more likely according to Eq. 6.3. Further, an increase of a_{r} rotates the gauge corner clockwise in Figure 6.5 which also should increase the likelihood of gauge corner contact. Also presented in **Paper D** is the meta-model for predicting median FI_{surf}

$$\begin{aligned}\widehat{FI} = &- 0.15 + 16\,a_{\mathrm{r}} + 4.3 \times 10^{-2} d_{\mathrm{r}} - 1.7 \times 10^{-2} e_{\mathrm{r}} - 16\,a_{\mathrm{w}} - 5.1 \times 10^{-2} d_{\mathrm{w}} \\ &+ 1.3 \times 10^{-2} e_{\mathrm{w}} - 1.7 \times 10^{-4} R_{\mathrm{c}} - 87\,a_{\mathrm{r}}^2 + 101\,a_{\mathrm{r}} a_{\mathrm{w}} \end{aligned} \quad (6.4)$$

where the curve radius R_{c} is in metres. By regarding the linear terms of the meta-model and their influence on the geometry (Figure 6.5), it seems that high $\widehat{FI}$ magnitudes are

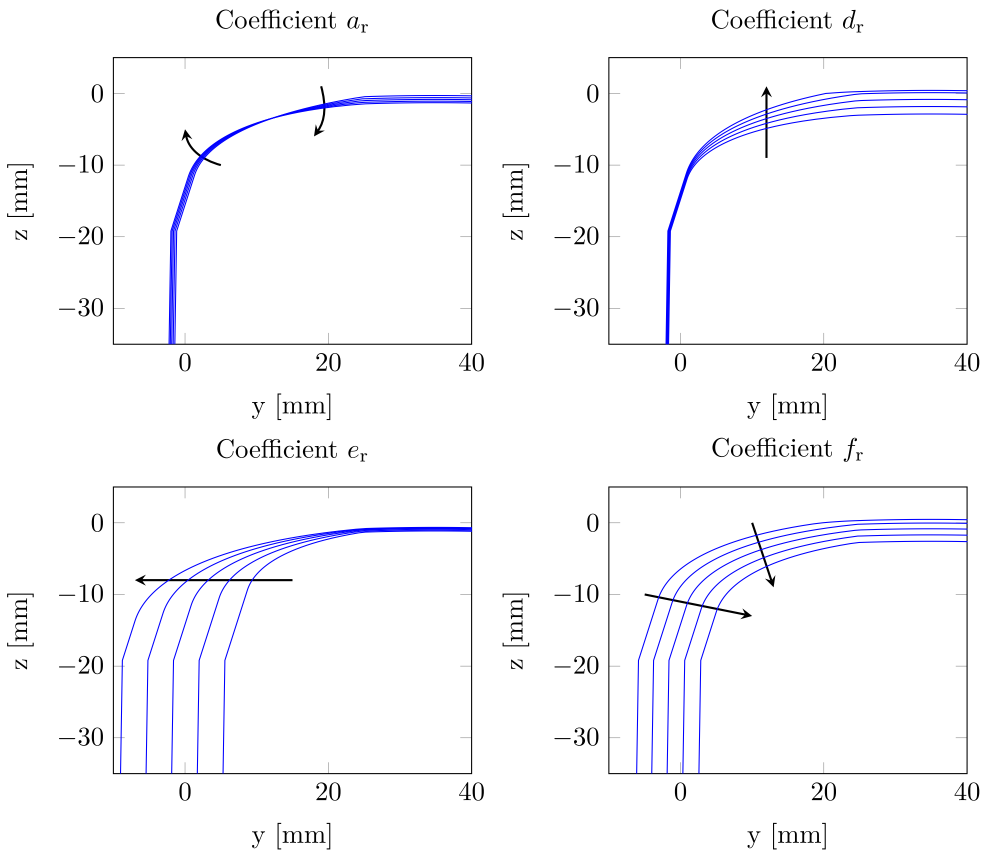

Figure 6.5: *Influence of an increase of a single coefficient of the parabolic solution to the general second degree equation (Eq. 5.1) on the gauge corner geometry. The arrows indicate how the shape of the parabola is influenced by an increase of the coefficient.*

promoted by contact low on the gauge corner (i.e closer to the gauge face). Furthermore, presented in **Paper D** is a meta-model predicting median $T\gamma$

$$\widehat{T\gamma} = 327 + 405\,a_\mathrm{r} + 10\,d_\mathrm{r} - 3.6\,e_\mathrm{r} - 14\,d_\mathrm{w} - 0.36\,R_\mathrm{c} - 0.34\,h_\mathrm{d} + 1.1 \times 10^{-4} R_\mathrm{c}^2 \qquad (6.5)$$

where the cant deficiency h_d is in millimetres.

To find out the generality of the meta-models presented in **Paper D** similar meta-models have been derived for a different vehicle model using the same method. The employed vehicle model is a generic locomotive which comes bundled with the multibody simulation package GENSYS. Some basic properties of the locomotive are presented in Table 4.1. The decision bound for the generic locomotive is the same as for the freight wagon given in Eq. 6.3. This is not surprising since the same wheel and rail profiles were used. The meta-model predicting surface initiated RCF becomes for the generic locomotive

$$\widehat{FI} = -0.26 + 23\,a_{\mathrm{r}} + 6.3\times10^{-2}\,d_{\mathrm{r}} - 2.8\times10^{-2}\,e_{\mathrm{r}} - 18\,a_{\mathrm{w}} - 7.2\times10^{-2}\,d_{\mathrm{w}} + 2.0\times10^{-2}\,e_{\mathrm{w}} - 8.2\times10^{-5}\,R_{\mathrm{c}} - 114\,a_{\mathrm{r}}^2 + 108\,a_{\mathrm{r}}a_{\mathrm{w}}. \tag{6.6}$$

The meta-model predicting $T\gamma$ is

$$\widehat{T\gamma} = 504 + 1307\,a_{\mathrm{r}} + 31\,d_{\mathrm{r}} - 13\,e_{\mathrm{r}} - 40\,d_{\mathrm{w}} - 0.38\,R_{\mathrm{c}} - 0.25\,h_{\mathrm{d}} + 1.2\times10^{-4}\,R_{\mathrm{c}}^2. \tag{6.7}$$

In Eq. 6.7 the terms h_{d} and R_{c}^2 may be not significant since their 95% significance intervals contain zero, however the significance intervals only just contain zero. Comparing the meta-models derived for a freight wagon and for a generic locomotive (i.e. Eq. 6.4 to Eq. 6.6; and Eq. 6.5 to Eq. 6.7) it is clear that the general appearance of meta-models is the same i.e. the signs of the coefficients are the same regardless of the vehicle model. Dividing the coefficients of the meta-models estimating $\widehat{FI}$ for the freight wagon with the corresponding coefficients of the meta-model for the generic locomotive (e.g. a_{r} from Eq. 6.4 divided by a_{r} from Eq. 6.6 etc.) reveals that the coefficients for rail and wheel geometries give quotients between 0.65 and 0.94 whereas the quotient for the curve radius is 2.1. This shows that the vehicle type has a rather large influence on all of the coefficients of the meta-model. The effect the non-equal wheel geometry quotients have on the rankings of wheel profiles based on Eq. 6.4 and Eq. 6.6 is presented in Figure 6.6. The lowest and highest ranked wheel profiles roughly keep their ranking regardless of the vehicle type. For profiles ranked in the range of 20 to 45 there are differences in the ranking depending on the vehicle type. However, the distribution of $\widehat{FI}$ magnitudes shows that intermediate magnitudes are the most common meaning that a small change in the $\widehat{FI}$ magnitude may lead to a large difference in ranking. Note that for maintenance planning purposes only the highest ranked profiles are of importance.

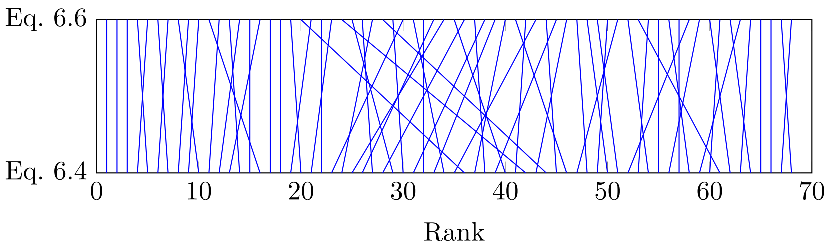

Figure 6.6: *Ranking of wheel profiles based on $\widehat{FI}$ magnitudes from Eq. 6.4 and Eq. 6.6. The lowest rank is given for lowest $\widehat{FI}$ magnitudes. A vertical line indicates that both equations rank the wheel profile equally.*

For the meta-models estimating $\widehat{T\gamma}$ (Eq. 6.5 and Eq. 6.7), the quotients of the rail and wheel coefficients are between 0.27 and 0.35. The quotients for the curve radius coefficients are 0.91 and 0.95, and the quotient for the cant deficiency coefficient is 1.36. This indicates that a meta-model derived for one vehicle type can be used qualitatively for another vehicle types.

An anti head check rail profile has been designed by Dollevoet [2010] to mitigate problems caused by head checks. One of the main features of the profile is that no contact occur at the gauge corner and thereby preventing head check formation. When the anti head check profile wears, the probability increases of contact occurring at the gauge corner. Decision bounds of the same type as Eq. 6.3 can here be used alone as an aid in maintenance decision making for track sections where anti head check profiles are installed. If a representative set of wheel profile parameters is available then a maintenance limit could e.g. be based on the percentage of wheels for which contact occurs at the gauge corner.

It should be noted that in the derivation of the meta-models (Eqs. 6.4 to 6.7), the contact areas are presumed to be (multi-point) Hertzian and resulting creep forces are evaluated with FASTSIM. The wheel/rail contact at the gauge corner may be conformal which violates assumptions of the Hertzian contact theory, see Section 4.1.

7 Main conclusions and future outlook

The thesis studies the degradation of wheels and rails mainly through dynamic multi-body simulations. In addition, operational damage patterns on locomotive wheels are investigated.

The following main conclusions can been drawn:

- Operational locomotive wheel damage and root causes
  - For the studied wheels RCF on the field side of the tread was most frequent.
  - Peak in the winter for reprofiling of wagon wheels was found, whereas for locomotive wheels the peak shifted to after rail grinding (late autumn to early winter). This indicates a profile mismatch introduced by grinding.
  - Additional root causes were identified as
    - → Increased number of wagons in a train.
    - → Higher braking efforts of locomotives.
    - → Seasonal variations in climate, grinding and lubrication.
  - An improved rail profile was introduced and preliminary results show some positive effects.
- Influence of track geometry on wheel/rail degradation
  - → For large radius curves an increase of the level of lateral track irregularities leads to an increase in RCF on both the high rail and the inner wheel.
  - → For small radius curves wear is likely to be the dominant form of damage on the high rail. An increase of lateral irregularities shifts the response to a mixed wear/RCF regime.
  - → Lateral irregularities in the wavelength span 10 to 50 metres have the largest influence on increasing RCF.

- Influence of wheel and rail profile geometries on wheel/rail degradation
    - Parametrisations schemes for wheel and rail profile geometries are presented.
        - → More compact storage of raw data.
        - → Parameters may be employed in comparisons of profiles.
    - Estimation of RCF and wear through meta-models.
        - → Most influential parameters are determined.
        - → Wheel and rail profiles can be ranked based on their ability to induce deterioration.
        - → Deterioration of profiles over time can be quantified from profile geometry measurements.

One of the main topics that should be considered for further research is to calibrate meta-models against observed wheel and rail damage magnitudes. After such a calibration, the intended use of the meta-models could be broadened to prediction of operational lives. Moreover, to incorporate track irregularities more thoroughly into the meta-models would be an interesting topic to pursue.

References

Andrade, A. and P. Teixeira (2011). Uncertainty in rail–track geometry degradation: Lisbon-Oporto line case study. *Journal of Transportation Engineering* 137 (3), 193–200. DOI: 10.1061/(ASCE)TE.1943-5436.0000206.

Arasteh khouy, I. et al. (2014). Cost-effective track geometry maintenance limits. *Proceedings of the Institution of Mechanical Engineers, Part F: Journal of Rail and Rapid Transit*. Advance online publication. DOI: 10.1177/0954409714542859.

Archard, J. (1953). Contact and rubbing of flat surfaces. *Journal of Applied Physics* 24 (8), 981–988. DOI: 10.1063/1.1721448.

Asplund, M. et al. (2014). Reliability and measurement accuracy of a condition monitoring system in an extreme climate: A case study of automatic laser scanning of wheel profiles. *Proceedings of the Institution of Mechanical Engineers, Part F: Journal of Rail and Rapid Transit* 228 (6), 695–704. DOI: 10.1177/0954409714528485.

Audley, M. and J. Andrews (2013). The effects of tamping on railway track geometry degradation. *Proceedings of the Institution of Mechanical Engineers, Part F: Journal of Rail and Rapid Transit* 227 (4), 376–391. DOI: 10.1177/0954409713480439.

Banverket (1998). *Räler – Krav på ny aoch begagnade. BVF 524.1.* in Swedish. 18 pp.

Beagley, T. (1976). Severe wear of rolling/sliding contacts. *Wear* 36 (3), 317–335. DOI: 10.1016/0043-1648(76)90110-1.

Becker, M. (1855). *Der Strassen- und Eisenbahnbau in seinem ganzen Umfange und mit besonderer Rücksicht auf die neuesten Constructionen.* in German. Stuttgart: Carl Mäcken Berlagsbuchhandlung.

Bogdañski, S. (2002). A rolling contact fatigue crack driven by squeeze fluid film. *Fatigue and Fracture of Engineering Materials and Structures* 25 (11), 1061–1071. DOI: 10.1046/j.1460-2695.2000.00563.x.

Bogojević, N., B. Dirks, et al. (2011). "Dynamic behaviour of freight wagons with three-piece bogie on Swedish Iron Ore Line". 22nd International Symposion on Dynamics of Vehicles on Roads and Tracks (IAVSD2011), Aug. 14–19 2011. Manchester, UK, 6 pp.

Bogojević, N., P. Jönsson, and S. Stichel (2011). "Iron ore transportation wagon with three-piece bogies – simulation model and validation". The 7th international scientific conference heavy machinery (HM2011), June 29–July 2 2011. Vrnjačka Banja, Serbia, 6 pp.

Bombardier (2008). *High power electric locomotives for hauling heavy ore trains – IORE Locomotives.* Brochure. Bombardier Transportation.

Bower, A. (1988). Influence of crack face friction and trapped fluid on surface initiated rolling contact fatigue cracks. *Journal of Tribology* 110 (4), 704–711. DOI: 10.1115/1.3261717.

Braghin, F. et al. (2006). A mathematical model to predict railway wheel profile evolution due to wear. *Wear* 261 (11-12), 1253–1264. DOI: 10.1016/j.wear.2006.03.025.

Burstow, M. (2004). *Whole life rail model application and development for RSSB – continued development of an RCF damage parameter.* Report. London, UK: Rail Safety & Standards Board. 74 pp.

Caprioli, S. (2014). "Thermal impact on rolling contact fatigue of railway wheels". PhD thesis. Gothenburg, Sweden: Chalmers University of Technology.

Carter, F. (1926). "On the action of a locomotive driving wheel". *Proceedings of the Royal Society of London A: Mathematical, Physical and Engineering Sciences.* Vol. 112. 760. The Royal Society, pp. 151–157.

CEN (2008). *Railway applications – Track – Track geometry quality – Part 1:Characterisation of track geometry. EN 13848-1:2003+A1:2008 (E).* European committee for standardization. 25 pp.

— (2010). *Railway applications – Track – Track geometry quality – Part 5:Geometric quality levels – Plain line. EN 13848-5:2008+A1:2010.* European committee for standardization. 22 pp.

— (2012). *Railway applications – Track – Track geometry quality – Part 6:Characterisation of track geometry quality. prEN 13848-6:22012.* European committee for standardization. 26 pp.

Chaar, N. (2007). "Wheelset structural flexibility and track flexibility in vechicle-track dynamic interaction". PhD thesis. Stockholm, Sweden: Royal Institute of Technology (KTH).

Cioppa, T. and T. Lucas (2007). Efficient Nearly Orthogonal and Space-Filling Latin Hypercubes. *Technometrics* 49 (1), 45–55. DOI: 10.1198/004017006000000453.

Deuce, R. (2007). *Wheel tread damage – an elementary guide.* Technical report 100115000. Netphen, Germany: Bombardier Transportation GmbH. 38 pp.

Dollevoet, R. (2010). "Design of an anti head check profile based on stress relief". PhD thesis. Enschede, The Netherlands: University of Twente. ISBN: 978-90-365-3073-6.

D-RAIL (2013). *D3.2 Analysis and mitigation of derailment, assessment and commercial impact.* Report. D-RAIL Consortium. 301 pp.

Ekberg, A. (2000). "Rolling contact fatigue of railway wheels – Towards tread life prediction through numerical modelling considering material imperfections, probabilistic loading

and operational data”. PhD thesis. Gothenburg, Sweden: Chalmers University of Technology.
Ekberg, A. (2009). “Fatigue of railway wheels”. *Wheel-Rail Interface Handbook*. Ed. by R. Lewis and U. Olofsson. Cambridge, UK: Woodhead Publishing, pp. 211–244. ISBN: 978-1-84569-412-8. DOI: 10.1533/9781845696788.1.34.
Ekberg, A. and E. Kabo (2005). Fatigue of railway wheels and rails under rolling contact and thermal loading – an overview. *Wear* 258 (7-8), 1288–1300. DOI: 10.1016/j.wear.2004.03.039.
Ekberg, A., E. Kabo, and H. Andersson (2002). An engineering model for prediction of rolling contact fatigue of railway wheels. *Fatigue and Fracture of Engineering Materials and Structures* 25 (10), 899–909. DOI: 10.1046/j.1460-2695.2002.00535.x.
Ekberg, A., E. Kabo, K. Karttunen, et al. (2014). Identifying the root causes of damage on the wheels of heavy haul locomotives and its mitigation. *Proceedings of the Institution of Mechanical Engineers, Part F: Journal of Rail and Rapid Transit* 228 (6), 663–672. DOI: 10.1177/0954409714526165.
Ekberg, A. and P. Sotkovszki (2001). Anisotropy and rolling contact fatigue of railway wheels. *International Journal of Fatigue* 23 (1), 29–43. DOI: 10.1016/S0142-1123(00)00070-0.
ERRI (1989). *ERRI B176 RP1, Preliminary studies and specifications – specification for a bogie with improved curving characteristics – specifications for a bogie with improved curving characteristics for body tilt.* Utrecht, Netherlands,
Esveld, C. (2001). *Modern railway track.* 2nd ed. Zaltbommel, The Netherlands: MRT–Productions. 654 pp. ISBN: 90-800324-3-3.
Fletcher, D., F. Franklin, and A. Kapoor (2009). “Rail surface fatigue and wear”. *Wheel – rail interface handbook.* Ed. by R. Lewis and U. Olofsson. Cambridge, UK: Woodhead publishing limited, pp. 280–310. ISBN: 978-1-84569-412-8.
Fröhling, R., U. Spangenberg, and G. Hettasch (2012). Wheel/rail contact geometry assessment to limit rolling contact fatigue initiation at high axle loads. *Vehicle System Dynamics* 50 (supp 1), 319–334. DOI: 10.1080/00423114.2012.665163.
Garnham, J. and C. Davis (2011). Very early stage rolling contact fatigue crack growth in pearlitic rail steels. *Wear* 271 (1–2), 100–112. DOI: 10.1016/j.wear.2010.10.004.
GENSYS (2010). *Release 1009.* Östersund, Sweden: AB DEsolver.
— (2014). *Release 1410.* Östersund, Sweden: AB DEsolver.
Grassie, S. (2012). Squats and squat-type defects in rails: The understanding to date. *Proceedings of the Institution of Mechanical Engineers, Part F: Journal of Rail and Rapid Transit* 226 (3), 235–242. DOI: 10.1177/0954409711422189.
Grassie, S. et al. (2012). Studs: A squat-type defect in rails. *Proceedings of the Institution of Mechanical Engineers, Part F: Journal of Rail and Rapid Transit* 226 (3), 243–256. DOI: 10.1177/0954409711421462.
Gustafsson, P. (2012). *Slitage och utmattning på Malmbanan.* in Swedish. Report 890855. Trafikverket. 94 pp.
Harker, M., P. O’Leary, and P. Zsombor-Murray (2008). Direct type-specific conic fitting and eigenvalue bias correction. *Image and Vision Computing* 26 (3), 372–381. DOI: 10.1016/j.imavis.2006.12.006.

Hertz, H. (1882). Ueber die Berührung fester elastischer Körper. *Journal für reine und angewandte Mathematik* 92, 156–171.
Heyder, R. and M. Brehmer (2014). Empirical studies of head check propagation on the DB network. *Wear* 314 (1), 36–43.
Hossein Nia, S., P. Jönsson, and S. Stichel (2014). Wheel damage on the Swedish iron ore line investigated via multibody simulation. *Proceedings of the Institution of Mechanical Engineers, Part F: Journal of Rail and Rapid Transit* 228 (6), 652–662. DOI: 10.1177/0954409714523264.
Ignesti, M. et al. (2014). Development of a model for the simultaneous analysis of wheel and rail wear in railway systems. *Multibody System Dynamics* 31 (2), 191–240. DOI: 10.1007/s11044-013-9360-0.
Jaiswal, J. (2009). *Characterisation of microstructural deformation as a function of rail grade*. Report D4.3.6. INNOTRACK. 30 pp.
Jendel, T. (1997). "Dynamic analysis of a freight wagon with modified Y25 bogies". MSc thesis. Deparment of Vehicle Engineering, KTH. 87 pp.
— (2002). Prediction of wheel profile wear - Comparisons with field measurements. *Wear* 253 (1-2), 89–99. DOI: 10.1016/S0043-1648(02)00087-X.
Johnson, K. (1985). *Contact mechanics*. English. Cambridge, UK: Cambridge Univ. Press. 447 pp. ISBN: 0521347963.
— (1989). The strength of surfaces in rolling contact. *Proceedings of the Institution of Mechanical Engineers. Part C. Journal of Mechanical Engineering Science* 203 (C3), 151–163. DOI: 10.1243/PIME_PROC_1989_203_100_02.
Kabo, E. et al. (2010). Rolling contact fatigue prediction for rails and comparisons with test rig results. *Proceedings of the Institution of Mechanical Engineers, Part F: Journal of Rail and Rapid Transit* 224 (4), 303–317. DOI: 10.1243/09544097JRRT343.
Kalker, J. (1979). Survey of wheel—rail rolling contact theory. *Vehicle System Dynamics* 8 (4), 317–358. DOI: 10.1080/00423117908968610.
— (1982). A Fast Algorithm for the Simplified Theory of Rolling Contact. *Vehicle System Dynamics* 11 (1), 1–13. DOI: 10.1080/00423118208968684.
— (1990). *Three-dimensional elastic bodies in rolling contact*. Dordrecht, The Netherlands: Kluwer Academic Publishers. 314 pp. ISBN: 0-7923-0712-7.
— (1991). Wheel-rail rolling contact theory. *Wear* 144 (1-2), 243–261. DOI: 10.1016/0043-1648(91)90018-P.
Kalousek, J. (2005). Wheel/rail damage and its relationship to track curvature. *Wear* 258 (7–8), 1330–1335. DOI: 10.1016/j.wear.2004.03.042.
Karttunen, K. (2015). "Estimation of gauge corner and flange root degradation from rail, wheel and track geometry". To be submitted for international publication.
Karttunen, K., E. Kabo, and A. Ekberg (2012). A numerical study of the influence of lateral geometry irregularities on mechanical deterioration of freight tracks. *Proceedings of the Institution of Mechanical Engineers, Part F: Journal of Rail and Rapid Transit* 226 (6), 575–586. DOI: 10.1177/0954409712445115.
— (2014a). Numerical assessment of the influence of worn wheel tread geometry on rail and wheel deterioration. *Wear* 317 (1-2), 77–91. DOI: 10.1016/j.wear.2014.05.006.
— (2014b). The influence of track geometry irregularities on rolling contact fatigue. *Wear* 314 (1-2), 78–86. DOI: 10.1016/j.wear.2013.11.039.

Kleijnen, J. P. et al. (2005). State-of-the-art review: a user's guide to the brave new world of designing simulation experiments. *INFORMS Journal on Computing* 17 (3), 263–289. DOI: 10.1287/ijoc.1050.0136.

Lewis, R. and R. Dwyer-Joyce (2004). Wear mechanisms and transitions in railway wheel steels. *Proceedings of the Institution of Mechanical Engineers, Part J: Journal of Engineering Tribology* 218 (6), 467–478. DOI: 10.1243/1350650042794815.

Lewis, R., R. Dwyer-Joyce, et al. (2010). Mapping railway wheel material wear mechanisms and transitions. *Proceedings of the Institution of Mechanical Engineers, Part F: Journal of Rail and Rapid Transit* 224 (3), 125–137. DOI: 10.1243/09544097JRRT328.

Lewis, R. and U. Olofsson (2004). Mapping rail wear regimes and transitions. *Wear* 257 (7–8), 721–729. DOI: 10.1016/j.wear.2004.03.019.

— (2009). "Basic tribology of the wheel—rail contact". *Wheel–Rail Interface Handbook*. Ed. by R. Lewis and U. Olofsson. Cambridge, UK: Woodhead Publishing, pp. 34–57. ISBN: 978-1-84569-412-8. DOI: 10.1533/9781845696788.1.34.

Li, Z. (2002). "Wheel-rail rolling contact and its application to wear simulation". PhD thesis. Technische Universiteit Delft. 118 pp. ISBN: 90-407-2281-1.

Magel, E. (2011). *Rolling contact fatigue: a comprehensive review.* Report DOT/FRA/ORD -11/24. Washington DC, USA: U.S. Department of Transportation – Federal railroad administration. 132 pp.

Magel, E. et al. (2003). The blending of theory and practice in modern rail grinding. *Fatigue and Fracture of Engineering Materials and Structures* 26 (10), 921–929.

MATLAB (2011). *Version 7.13.0 (R2011b).* Natick, Massachusetts: The MathWorks Inc.

Nerman, G. (1856). *Afhandling om jernvägars anläggning och rörelsematerial.* in Swedish. Stockholm, Sweden: Alb. Bonnier's Förlag.

Nilsson, R. (2005). "On wear in rolling/sliding contacts". PhD thesis. Stockholm, Sweden: Department of Machine Design, Royal Institute of Technology (KTH).

Olofsson, U. and T. Telliskivi (2003). Wear, plastic deformation and friction of two rail steels – a full-scale test and a laboratory study. *Wear* 254 (1-2), 80–93. DOI: 10.1016/S0043-1648(02)00291-0.

ORE (1988). *Question D 161. Final report – conclusions and recommendations.* Report. Utrecht, Netherland: Office for Research and Experiments of the International Union of Railways. 48 pp.

Paderno, C. (2009). "Simulation of ballast behaviour under traffic and tamping process". 9th Swiss Transport Research Conference, Sept. 9–11 2009. Monte Verità/Ascona, Switzerland, 22 pp.

Pearce, T. and N. Sherratt (1991). Prediction of wheel profile wear. *Wear* 144 (1-2), 343–351. DOI: 10.1016/0043-1648(91)90025-P.

Pombo, P. et al. (2011). Development of a wear prediction tool for steel railway wheels using three alternative wear functions. *Wear* 271 (1–2), 238–245. DOI: 10.1016/j.wear.2010.10.072.

Pålsson, B. and J. Nielsen (2012). Wheel-rail interaction and damage in switches and crossings. *Vehicle System Dynamics* 50 (1), 43–58. DOI: 10.1080/00423114.2011.560673.

RSSB (2010). *Trials of wheel and rail rolling contact fatigue control measures – site monitoring and sustainable operation limits.* Report. London, UK: Rail Safety & Standards Board. 58 pp.

Schilke, M., N. Larijani, and C. Persson (2014). Interaction between cracks and microstructure in three dimensions for rolling contact fatigue in railway rails. *Fatigue & Fracture of Engineering Materials & Structures* 37 (3), 280–289. DOI: 10.1111/ffe.12112.

Smith, R. A. (2003). The wheel–rail interface—some recent accidents. *Fatigue & Fracture of Engineering Materials & Structures* 26 (10), 901–907. ISSN: 1460-2695. DOI: 10.1046/j.1460-2695.2003.00701.x.

Steenbergen, M. and R. Dollevoet (2013). On the mechanism of squat formation on train rails - Part I: Origination. *International Journal of Fatigue* 47, 361–372. DOI: 10.1016/j.ijfatigue.2012.04.023.

Stock, R. and R. Pippan (2014). Rail grade dependent damage behaviour - Characteristics and damage formation hypothesis. *Wear* 314 (1-2), 44–50. DOI: 10.1016/j.wear.2013.11.029.

Stone, D. (2004). *Atlas of wheel and rail defects*. International Union of Railways (UIC). 48 pp. URL: http://www.uic.org.

Suh, N. P. (1973). The delamination theory of wear. *Wear* 25 (1), 111–124. DOI: 10.1016/0043-1648(73)90125-7.

Telliskivi, T. and U. Olofsson (2001). Contact mechanics analysis of measured wheel-rail profiles using the finite element method. *Proceedings of the Institution of Mechanical Engineers, Part F: Journal of Rail and Rapid Transit* 215 (2), 65–72. DOI: 10.1243/0954409011531404.

Trafikverket (2012). *Säkerhetsbesiktning av fasta järnvägsanläggningar. BVF 807.2.* in Swedish. 2.0. 114 pp.

Tunna, J., J. Sinclair, and J. Perez (2007). A Review of wheel wear and rolling contact fatigue. *Proceedings of the Institution of Mechanical Engineers, Part F: Journal of Rail and Rapid Transit* 221 (2), 271–289. DOI: 10.1243/0954409JRRT72.

UIC (2002). *Rail defects. UIC Code 712 R, 4th edn.* Paris, france: International Union of Railways (UIC). 111 pp.

— (2009). *Testing and approval of railway vehicles from the point of view of their dynamic behaviour – safety – track fatigue – running behaviour. Leaflet 518, 4th edn.* International Union of Railways (UIC). 126 pp. URL: http://www.uic.org.

Vollebregt, E., S. Iwnicki, et al. (2012). Assessing the accuracy of different simplified frictional rolling contact algorithms. *Vehicle System Dynamics* 50 (1), 1–17. DOI: 10.1080/00423114.2011.552618.

Vollebregt, E. and G. Segal (2014). Solving conformal wheel-rail rolling contact problems. *Vehicle System Dynamics* 52 (SUPPL. 1), 455–468. DOI: 10.1080/00423114.2014.906634.

Zhao, X. and Z. Li (2015). A three-dimensional finite element solution of frictional wheel–rail rolling contact in elasto-plasticity. *Proceedings of the Institution of Mechanical Engineers, Part J: Journal of Engineering Tribology* 229 (1), 86–100. DOI: 10.1177/1350650114543717.

Zobory, I. (1997). Prediction of wheel/rail profile wear. *Vehicle System Dynamics* 28 (2-3), 221–259. DOI: 10.1080/00423119708969355.